



University of  
Massachusetts  
Amherst

## Development of an Oriented- Eddy Collision Model for Turbulence

Item Type	Thesis (Open Access)
Authors	Andeme, Raeann
DOI	<a href="https://doi.org/10.7275/610551">10.7275/610551</a>
Download date	2026-04-21 23:33:01
Link to Item	<a href="https://hdl.handle.net/20.500.14394/45096">https://hdl.handle.net/20.500.14394/45096</a>

**DEVELOPMENT OF AN ORIENTED-EDDY COLLISION MODEL FOR  
TURBULENCE**

A Thesis Presented

by

RaeAnn Andeme

Submitted to the Graduate School of the  
University of Massachusetts Amherst in partial fulfillment  
of the requirements for the degree of

**MASTER OF SCIENCE IN MECHANICAL ENGINEERING**

September 2008

Department of Mechanical and Industrial Engineering

© Copyright by RaeAnn Andeme 2008

All Rights Reserved

**DEVELOPMENT OF AN ORIENTED-EDDY COLLISION MODEL FOR  
TURBULENCE**

A Thesis Presented

by

**RAEANN ANDEME**

Approved as to style and content by:

---

Blair J. Perot, Chair

---

Ian Grosse, Member

---

Stephen de Bruyn Kops, Member

---

Mario Rotea, Department Head  
Mechanical and Industrial Engineering

## **DEDICATION**

To my loving parents Dr. Bernard and Anne Boum who were always present in time of need. Thanks for their continual emotional support, their firm and yet gentle guidance.

They taught me that one way to overcome adversity is to try harder. Great Thanks to  
GOD for the spiritual guidance he's provided me through them.

## ACKNOWLEDGEMENTS

I would like to first thank my thesis advisor Blair J. Perot for his years of patient guidance and support. Thanks are also due to my thesis committee members, Stephen de Bruyn Kops and Ian Grosse for their helpful comments and advice during all phases of my research. We all gratefully acknowledge the financial support of the Office of Naval Research (N00014-04-1-0267) under the supervision of Dr. Ronald Joslin.

On a personal note, I wish to express my love and gratitude to my close family: This is my husband Marius Tawembe, my two brothers Joel and Ivan and my grandparents Fred and Nancy Stine. None of this would have been possible without their constant love and encouragement.

Thanks to Dorothy Adams, who provided assistance with The Graduate School bureaucracy including rules, regulations and endless forms.

I would also like to extend my gratitude to my lab companions: together their friendship and support have greatly contributed to my academic advancement. I wish them all the best of luck in their academic and professional goals.

Finally, a special thank you to all those whose support and friendship provided me with the necessary encouragement when the goal got blurry.

## **ABSTRACT**

DEVELOPMENT OF AN ORIENTED-EDDY COLLISION MODEL

SEPTEMBER 2008

RAEANN ANDEME, M.S., UNIVERSITY OF MASSACHUSETTS AMHERST

Directed by: Professor Blair J. Perot

The exact governing equations of fluid dynamics are too computationally expensive to solve on a computer for practical applications. Hence, it is currently not possible to analytically describe the behavior of a turbulent flow -in particular its internal structures-, making turbulence one of the major remaining unsolved problems in Classical Physics. One solution to computationally predict the performance of engineering applications involving fluids is the formulation of alternative and computationally tractable equations. This work demonstrates the feasibility of modeling turbulence as a collection of interacting particles with intrinsic orientation. It also discusses current efforts regarding its accuracy and computational overhead in numerous turbulent flows. The goal of this thesis is to focus on numerical implementation as well as model evaluation and validation. The Oriented-Eddy Collision Model is tested for basic flow cases and incorporated inhomogeneity. The project is successful in demonstrating that with appropriate extensions, the model can be applied to a very wide variety of turbulent flows with high predictive accuracy.

# TABLE OF CONTENTS

	Page
ACKNOWLEDGMENTS.....	v
ABSTRACT.....	vi
LIST OF TABLES.....	ix
LIST OF FIGURES.....	x
LIST OF SYMBOLS.....	xiii
CHAPTER	
1. INTRODUCTION.....	1
2. ORIENTED EDDY COLLISION MODEL.....	4
2.1. Summary.....	4
2.2. Oriented Eddy Collision Model Advantages.....	4
2.3. Oriented Eddy Collision Model Equations.....	5
2.4. Two Point Correlation Equations.....	8
3. NUMERICAL RESULTS.....	11
3.1. Isotropic Decay Simulations.....	11
3.1.1. Isotropic Decay.....	12
3.1.2. Kinetic Energy.....	16
3.1.3. Rotating Decaying Grid-Turbulence.....	23
3.2. Rapid Distortion Theory.....	35
3.3. Return-to-Isotropy Models.....	40
3.3.1. R-return models.....	41
3.3.2. K-return models.....	42

3.4. Shear/Strain Flows.....	44
3.5. Numerical Results: return-to-isotropy and shear/strain deformation.....	44
3.6. Diffusion.....	49
4. CONCLUSIONS.....	57
REFERENCES.....	58

## LIST OF TABLES

Tables	Page
1. Research Summary.....	11
2. Initial conditions.....	17
3. Rotation-models along with their respective tuning constants $C_1$ and $C_2$ .....	24
4. Initial conditions of Mansour, Cambon & Speziale, Jacquin and Blaisdell.....	24
5. Wigeland & Nagib's initial conditions.....	25
6. Initial conditions of Shimomura, de Bruyn Kops and Veeravalli.....	25
7. Initial conditions of Matsumoto, Lee & Reynolds and Blaisdell.....	35
8. Tensor matrix for simple deformations.....	36
9. Matsumoto and Le Penven summary using (Rotta-L, $K_{ij}$ ), which is $(D_{ij}^A, m_i^A)$ ...	44
10. Hallback's summary using (Rotta-L, $K_{ij}$ ) for Plane Strain.....	44

## LIST OF FIGURES

Figure	Page
1. Oriented-Eddy Collision Illustration.....	4
2a. $R_{11}$ , $R_{22}$ and $R_{33}$ as seen from the $r_3$ -direction.....	9
2b. A planar slice of a three dimensional $R_{11}$ and $R_{22}$ two-point correlation in the X-Y plane about $Z=0$ .....	10
3. Power-law exponent as a function of the turbulent Reynolds number for a $\hat{k}^2$ low wavenumber spectrum.....	13
4. Power law exponent as a function of Reynolds number for a $\hat{k}^4$ low wavenumber spectrum.....	15
5. Wigeland and Nagib's decaying kinetic energy.....	18
6. Mansour, Cambon and Speziale's decaying kinetic energy.....	19
7. Jacquin's decaying kinetic energy.....	20
8. de Bruyn Kops's decaying kinetic energy.....	21
9. Squires' decaying kinetic energy for both $\hat{k}^2$ and $\hat{k}^4$ .....	22
10. Performance comparison of $k$ , $\omega$ and $k$ -smooth rotation terms.....	26
11. Performance comparison of $k$ , $\omega$ and $k$ -smooth rotation terms based on Mansour, Cambon and Speziale experimental data .....	27
12. Performance comparison of $k$ , $\omega$ and $k$ -smooth rotation terms based on Mansour, Cambon and Speziale's experimental data.....	28
13. Performance comparison of $k$ , $\omega$ and $k$ -smooth rotation terms for Blaisdell. (homogeneous shear flow).....	29
14. Rotating isotropic decay of Wigeland & Nagib using the rotation model $n_i^C$ . Turbulent kinetic energy versus time.....	30
15. Rotating Isotropic decay of Jacquin. Turbulent kinetic energy versus time. ....	31
16. Rotating isotropic decay of Shimomura. Turbulent kinetic energy versus time.....	32

17. de Bruyn Kops rotating decaying turbulence. Turbulent kinetic energy versus time.....	33
18. Veeravalli's decaying kinetic energy. Kinetic energy versus time.....	33
19. Rotating isotropic decay of Mansour, Cambon and Speziale. Turbulent kinetic energy versus time. a) $Re_T=27.2$ and b) $Re_T=67.1$ .....	34
20. Lee & Reynolds' axisymmetric contraction. The dots represent the DNS and the lines represent the OEC model prediction. $SK/\epsilon=55.9$ .....	36
21. Lee & Reynolds' axisymmetric expansion. The dots represent the DNS and the lines represent the OEC model prediction. $SK/\epsilon=9$ .....	37
22. Lee & Reynolds' plane strain. The dots represent the DNS and the lines represent the OEC model prediction. $SK/\epsilon=4$ .....	37
23. Matsumoto's shear deformation. The dots represent the DNS data and the lines represent the OEC model prediction. The large imposed strain ( $SK/\epsilon=30.6$ ) implies RDT is closely approximated. ....	38
24. Blaisdell's elliptical flow with a) return model on, b) rotation model on and c) both return and rotation models on.....	39
25. Blaisdell's elliptical flow: RDT.....	40
26. $m_i^A$ and $m_i^B$ model comparisons.....	43
27. Le Penven - case A. a) Reynolds stresses and b) Kinetic energy.....	45
28. Le Penven - case B. a) Reynolds stresses and b) Kinetic energy.....	46
29. Matsumoto's shear deformation. The dots represent his DNS and the lines represent our model prediction. a) Reynolds stresses and b) Dissipation and kinetic energy.....	47
30. Hallback – Plane Strain a) $S=3$ and b) $S=1$ .....	48
31. Eddy viscosity comparison for both global equations.....	50
32. Kinetic energy versus position at different times t. Chasnov at $t=0$ . The stars represent data from Chasnov and the solid blue line corresponds to our interpolation. ....	52
33. Kinetic Energy versus position at different times t. The matching blue lines correspond to the OEC simulations. a) linear-linear plot and	

b)log-linear plot.....	53
34. $R_{11}$ (kinetic energy component) versus position. The stars represent data from Gilbert at times $t=0, 0.0292, 0.0402, 0.0764, 0.0884, 0.1154, 0.1274, 0.1634$ and $0.2024$ seconds. The matching solid lines correspond to the OEC simulations. ....	54
35. Kinetic Energy versus position at different times $t$ . The stars represent data from Carati at times $t=0, 0.071$ and $0.191$ seconds. The matching solid lines correspond to our simulations. ....	55
36. Dissipation versus position at different times $t$ . The stars represent data from Carati at times $t=0, 0.071$ and $0.191$ seconds. The matching solid lines correspond to our simulations. ....	56

## LIST OF SYMBOLS OR ABBREVIATIONS

$\hat{k}$	Disk Orientation Vector
$k_i$	Orientation Vector Length
$k_{i,t}$	Time Derivative, Disk Orientation Vector
$\hat{k}^2, \hat{k}^4$	Low Wave Number of the Energy Spectrum
$k^2$	Square of the Orientation Vector Length
$K$	Total Kinetic Energy
$\hat{K}$	Total Kinetic Energy Vector
$\sum$	Summation
$N$	Number of Orientations
$\hat{R}_{ij}$	Individual Reynolds Stress Vector
$R_{ij}$	Total Reynolds Stress
$\hat{R}_{ij,t}$	Time Derivative, Individual Reynolds Stress Vector
$\varepsilon$	Dissipation
$K_{,t}$	Time Derivative, Kinetic Energy
$\varepsilon_0, K_0$	Initial Dissipation, Initial Kinetic Energy
$Re_T$	Turbulent Reynolds Number
$Ro_T$	Turbulent Rossby Number
$t$	Time
$n$	Decay Exponent
$\frac{1}{\tau_R}, \frac{1}{\tau_K}$	High Reynolds Number Timescale Factors
$\vec{r}$	Distance Vector Between Two Points
$R_{11}, R_{22}, R_{33}$	Auto-Correlation in the x, y and z direction
$S$	Strain Tensor
$\infty$	Infinity
$\left(\frac{\rho}{\tau_K}\right), \left(\frac{\rho}{\tau_R}\right)$	High Reynolds Number Timescale Factor, Vectors
$\bar{u}_{i,k}$	Fluid Rotation
$\bar{u}_{l,k}^*$	System Rotation
$\Omega_k$	Rotation Vector for a non-inertial Frame
$\delta_{il}$	Kronecker Delta
$D_{ij}$	Return-to-Isotropy model
$n_i$	Rotation Term

$m_i$	k-Return Model
$\nu$	Eddy Viscosity
$\nu_T$	Turbulent Viscosity
$\alpha_L, \alpha_H$	Tuning Constants (OEC Model)
$p, q, l$	Tuning Constants (Time Scale)
$C_1, C_2$	Tuning Constants (Rotation Model)
$C_R, C_{K1}, C_{K2}$	Tuning Constants (Return-to-Isotropy Model)
$C_L$	Tuning Constant (Diffusion)

# CHAPTER 1

## INTRODUCTION

In the book *Computational Methods for Fluid Dynamics*, Ferziger and Peric define fluids “as substances whose molecular structure offers no resistance to external shear flow.” The governing equations of fluid dynamics, the Navier-Stokes equations, define the evolution of mass, momentum and energy of fluid flows whether the flow is laminar, transitional or turbulent. In fluid dynamics, turbulence is a flow regime characterized by chaotic fluid variations such as energy and dissipation. Turbulent flows represent most flows encountered in engineering practice and therefore carry some importance. There are multiple applications of turbulent flows such as the dispersion of pollutants in the atmosphere, weather prediction, channel flow, internal combustion engines, gas turbines, external flow over airplanes, submarines.

It is currently not possible to analytically describe the behavior of a turbulent flow -in particular its internal structures-, making turbulence one of the major remaining unsolved problems in Classical Physics. However, there are some known approaches to predicting turbulent flows. The first one involves the use of correlations such as the ones that give the friction factor as a function of the Reynolds number. This method is limited to extremely simple flows that are characterizable by just a few parameters. The down-side of this approach is the lack of flexibility. Currently, the three main approaches that are extensively used by Computational Fluid Dynamics (CFD) users and researchers are the Reynolds-averaged Navier-Stokes (or RANS) equations, Direct Numerical Simulation (DNS) and Large Eddy Simulation (LES). RANS is a method based on equations obtained by averaging the equations of motion over ensembles. This is equivalent to time

averaging in a statistically steady flow or spatial averaging over a coordinate in which the statistics do not vary. The RANS equations do not form a closed set and thus require the introduction of approximations of the Reynolds stresses. RANS provides the engineer with only the average properties of a turbulent flow such as the average forces on a body, the degree of mixing between two incoming streams of fluids, or in chemical engineering the reacted amount of some substance. The RANS equations are very similar to the governing Navier-Stokes equations except for the unknown Reynolds stress tensor.

As of today, the most accurate approach to turbulence solution is Direct Numerical Simulations. DNS is very useful in extracting specific information such as the kinetic energy or the dissipation rate. This approach solves the Navier-Stokes equations for all of the motions in a turbulent flow and therefore, does not involve any approximation or averaging other than numerical errors. However, the computational cost of DNS is very high and increases rapidly with higher Reynolds numbers. For the Reynolds numbers encountered in most industrial applications, the computational resources required by a DNS would exceed the capacity of the most powerful computer available in 100 years. However, direct numerical simulation is a useful tool in fundamental research in turbulence. In addition, DNS is useful in the development of turbulence models for practical applications. Results obtained from DNS are extremely detailed, making DNS a very expensive and inappropriate tool for engineering design.

Finally, LES compromises between one point closure methods -like RANS- and direct solution methods such as DNS. This technique solves for the largest scale motions while modeling only the small scale motions. Because the large scale motions generally contain more energy than the small scale ones, this approach can capture much of the

actual physics using first principles. LES is three dimensional, time dependent and less expensive than DNS. DNS is useful in developing LES since it allows for both “a priori” (the input data for the model is taken from a DNS simulation) and "a posteriori" tests (the results produced by the model are compared to those obtained by DNS). In our research, DNS, LES and experimental results are used in developing the Oriented Eddy Collision (OEC) model for predicting turbulence.

## CHAPTER 2

### ORIENTED-EDDY COLLISION MODEL

#### 2.1. Summary

This thesis demonstrates the feasibility of modeling turbulence as a collection of interacting (colliding) particles with intrinsic orientation as shown in Figure 1 below:



Figure 1: Oriented-Eddy Collision Illustration

The model tracks the average behavior of each of these particles. Previous work has shown that the eddy collision model can capture important physical processes (such as fast pressure-strain effects and strong inhomogeneity) using no model constants. The remaining important physical processes (slow pressure-strain and the return to isotropy) can be captured by adding information and additional terms to the collision model. This thesis continues the work of Chartrand (*Eddy Collision Models for Turbulence*<sup>64</sup>), on the development of the Oriented Eddy Collision Model and also tests its accuracy and computational overhead in numerous turbulent flows. We focus on the numerical implementation as well as the model evaluation and validation. In addition, we tested the model for basic flow cases and incorporated inhomogeneity by deriving and implementing the rotation and diffusion terms adapted to the eddy collision model in our code.

## 2.2. Oriented Eddy Collision Model Advantages

The collision model approach has a number of advantages over classic Reynolds stress transport (RST) models. For instance, the collision model is an approach to two-point correlation equations while RANS is a single-point correlation approach. In addition, mathematical constraints like realisability are automatically satisfied and a wider variety of models can be envisioned. In addition, because the approach is different, new insights into old problems can be obtained. The un-oriented collisional approach retain the difficulties of RST models, In particular, two critical parts of the model, the fast pressure-strain term and the dissipation transport equation, still require complex modeling terms with multiple model ‘constants’. By allowing eddies to have an orientation as in the current approach, these difficulties are removed. The orientation is the reason why RDT and rapid pressure-strain can be captured exactly (see Chartrand<sup>64</sup> pp.15-16). It allows the model to specifically represent how eddies stretch and deform.

In summary, after testing numerous models for numerous flow cases, we can say that the oriented eddy collision model is:

- More predictive than RANS
- Computationally achievable
- Uses fewer model constants than RANS
- Is more expensive than RANS, but less expensive than DNS

## 2.3. Oriented Eddy Collision Model Equations

Two main equations are used to represent the oriented collision model. The first one represents  $\hat{R}_{ij}$ , which is the Reynolds stress (average velocity fluctuations) for one

orientation  $k_i$  (see equation 2.3.2 below). The orientation vector,  $k_i$ , has units of 1/length and captures the eddy size and orientation.

$$\begin{aligned} \hat{R}_{ij,t} = & \hat{R}_{jk} \left[ \bar{u}_{i,k} + 2\bar{u}_{i,k}^* \left( \frac{k_j k_l}{k^2} - \delta_{jl} \right) \right] + \hat{R}_{ik} \left[ \bar{u}_{j,k} + 2\bar{u}_{j,k}^* \left( \frac{k_j k_l}{k^2} - \delta_{jl} \right) \right] \\ & - \left( \alpha_L \nu k^2 + \alpha_H \frac{1}{\tau_R} \right) \hat{R}_{ij} - \alpha_H \left( \frac{1}{\tau_R} \right) D_{ij} - \frac{1}{\tau_R} n_i + \left( \hat{R}_{lj} \frac{k_i}{k^2} + \hat{R}_{li} \frac{k_j}{k^2} \right) m_l + \nabla(\nu + \nu_T) \nabla \hat{R}_{ij} \end{aligned} \quad (2.3.1)$$

where

$$\left( \frac{1}{\tau_R} \right) = \left( \frac{1}{\tau_K} \right) = K^{\frac{1}{2}} \left( \frac{N\hat{K}}{K} \right)^{q/2} |k| \left( \frac{k}{k} \right)^p \quad (2.3.2)$$

The total Reynolds stress defined as  $R_{ij}$  is the averaged sum of the individual  $\hat{R}_{ij}$ , meaning  $R_{ij} = \frac{1}{N} \Sigma \hat{R}_{ij}$ . Equation (2.3.1) has seven grouped terms. The mean flow gradients and system rotation is accounted for by  $\bar{u}_{i,k}^* = \bar{u}_{i,k} + e_{ikj} \Omega_k$ , with  $\Omega_k$  being the rotation vector for a non-inertial frame. The dissipative behavior of the model is captured by  $\left( \alpha_L \nu k^2 + \alpha_H \frac{1}{\tau_R} \right) \hat{R}_{ij}$  and  $\alpha_H \left( \frac{1}{\tau_R} \right) D_{ij}$  is the return-to-isotropy model discussed in section 3.3 below. The factor  $\left( \frac{1}{\tau_R} \right)$  is the timescale used to model the dissipation.  $\frac{1}{\tau_R} n_i$  is the rotation term. The sixth term  $\left( \hat{R}_{lj} \frac{k_i}{k^2} + \hat{R}_{li} \frac{k_j}{k^2} \right) m_l$  arises from the need to maintain orthogonality ( $R_{ij} k_i = 0$ ) between the orientations and the  $\hat{R}_{ij}$  ( $m_l$  is the k-return model). Incompressibility requires  $R_{ij} k_i = 0$ . The final term  $\nabla(\nu + \nu_T) \nabla \hat{R}_{ij}$  models the diffusive action of the Reynolds stresses.

The second equation represents the orientation  $k_i$  with its time-derivative defined as:

$$k_{i,t} = -k_k \bar{u}_{k,i} - \frac{1}{l} \left( \alpha_L \nu k^2 + \alpha_H \frac{1}{\tau_R} \right) k_i + \frac{1}{\tau_R} n_i + \left( \frac{1}{\tau_R} \right) m_i + \nabla(\nu + \nu_T) \nabla k_i \quad (2.3.3)$$

The above equation contains six grouped terms. The first term captures the mean gradient effects (shear). This term is the equation for passive disks. Just as in (2.3.1), the second term captures the dissipation;  $l$  takes on the value 3 or 5 respectively for the  $\hat{k}^2$  or  $\hat{k}^4$  low wave number. The third term  $n_i$  present in  $\frac{1}{\tau_R} n_i$  models the secondary rotation effects and  $m_i$  is the return model for the orientations. The last term,  $\nabla(\nu + \nu_T)\nabla k_i$  accounts for the diffusive action of the orientation vectors  $k_i$ .

In addition, the general formula for dissipation is:

$$\varepsilon = -K_{,t} \quad (2.3.4)$$

and

$$K_{,t} = \sum \hat{R}_{ik} [\bar{u}_{i,k} - 2\bar{u}_{i,k}^*] - \alpha_L \nu \sum k^2 \hat{K} - \alpha_H \sum \left(\frac{1}{\tau_R}\right) D_{ij} \quad (2.3.5)$$

Hence,

$$\varepsilon = \sum \hat{R}_{ik} [2\bar{u}_{i,k}^* - \bar{u}_{i,k}] + \alpha_L \nu \sum k^2 \hat{K} + \alpha_H \sum \left(\frac{1}{\tau_R}\right) D_{ij} \quad (2.3.6)$$

With isotropy present, the first term of equation (2.3.6) disappears, resulting in

$$\varepsilon = \sum \left[ \alpha_L \nu \bar{k}^2 K + \alpha_H \left(\frac{1}{\tau_R}\right) D_{ij} \right] \quad (2.3.7)$$

where

$$K = \sum \hat{K} \quad (2.3.8)$$

$$\bar{k}^2 = \frac{1}{N} \sum k^2 \quad (2.3.9)$$

## 2.4. Two point correlation equation

The unknowns in the oriented eddy model are closely related to the two-point correlations. In this section, we take a brief look at this relationship.

Assuming

$$R_{ij}(\vec{x}, \vec{r}) \approx \sum \hat{R}_{ij} F(\vec{k} \cdot \vec{r}) \quad (2.4.1)$$

where  $F(\eta)$  is a simple function of  $\vec{r}$ , the distance between two points.

Considering the specific case where  $F(\vec{k}, \vec{r}) = e^{-|\vec{k} \cdot \vec{r}|}$ ,

$$R_{ij}(\vec{x}, \vec{r}) = \sum \hat{R}_{ij} e^{-|\vec{k} \cdot \vec{r}|} \quad (2.4.2)$$

When looking at the two-point correlation in the x-direction for example, we get

$$R_{11}(r_1, r_2, r_3) \approx \sum \hat{R}_{11} e^{-|k_1 r_1 + k_2 r_2 + k_3 r_3|} \quad (2.4.3)$$

Similarly for R22 and R33:

$$R_{22}(r_1, r_2, r_3) \approx \sum \hat{R}_{22} e^{-|k_1 r_1 + k_2 r_2 + k_3 r_3|} \quad (2.4.4)$$

$$R_{33}(r_1, r_2, r_3) \approx \sum \hat{R}_{33} e^{-|k_1 r_1 + k_2 r_2 + k_3 r_3|} \quad (2.4.5)$$

Hence, we obtained the contour plots shown in Figure 2a:

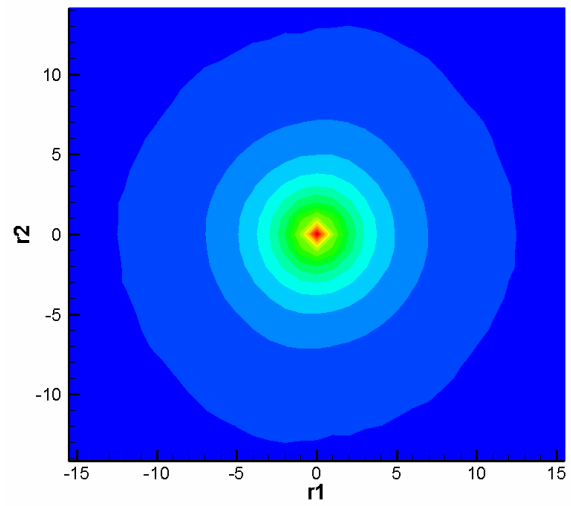
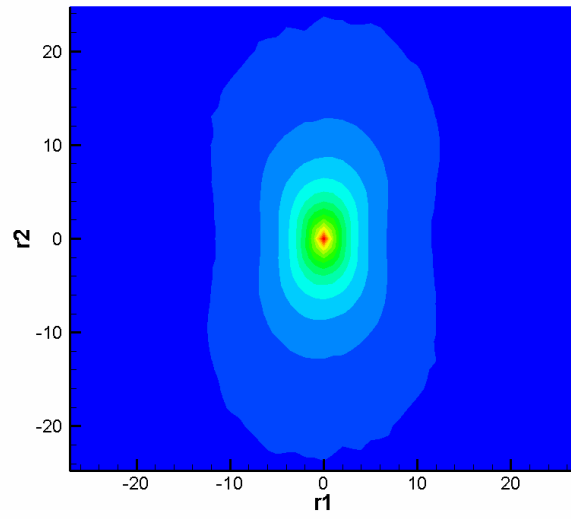
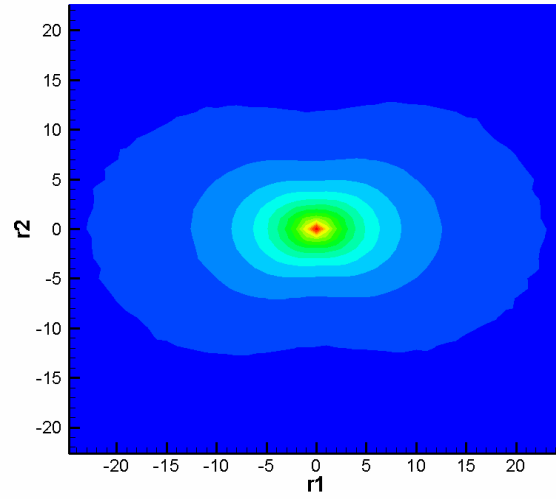


Figure 2a:  $R_{11}$ ,  $R_{22}$  and  $R_{33}$  as seen from the  $r_3$ -direction.

DNS two-point correlation data corresponding to the first two figures above (OEC model) is shown below in Figure 2b. The shapes are very similar. The mesh size used in the DNS simulation was 768 by 768 by 1536 cells, with a domain size of 56.54 by 56.54 by 113.09 centimeters.

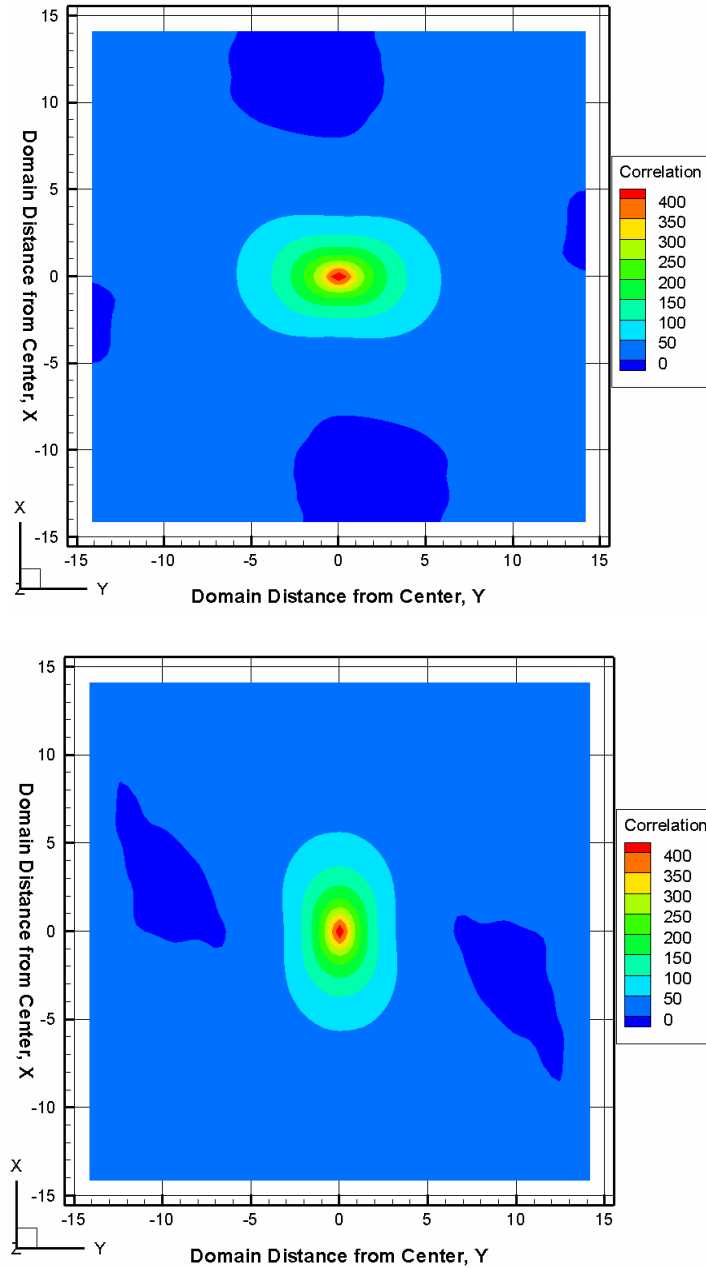


Figure 2b: A planar slice of a three dimensional  $R_{11}$  and  $R_{22}$  two-point correlation in the X-Y plane about  $Z=0$ .

Hence, the similarity of Figures 1a and 1b above validates the OEC model.

## CHAPTER 3

### NUMERICAL RESULTS

Below is the table that summarizes the different sections and results of the current project.

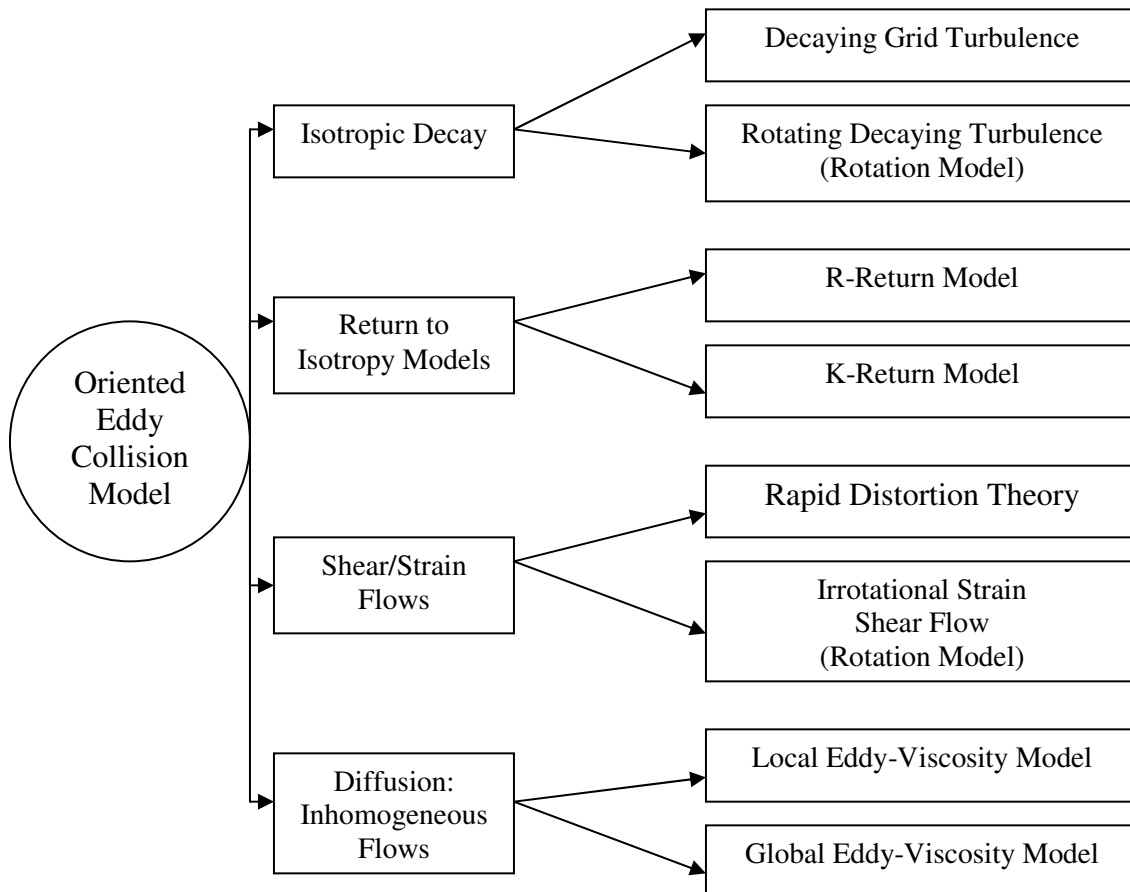


Table 1: Research Summary

#### 3.1. Isotropic Decay Simulations

In general, when the properties of a material are the same in all directions, the material is said to be isotropic. In the case of turbulence, if the fluctuations are independent of direction, the turbulence is isotropic. When the fluctuations do not have

any directional preference, then the off-diagonal components of  $R_{ij}$  vanish, and

$$R_{11} = R_{22} = R_{33}. \text{ Mathematically, this corresponds to } R_{ij} = \frac{2}{3} K \delta_{ij}.$$

In this work, it is necessary to define isotropy for the orientations as well. For isotropy, all orientation vectors have the same magnitude and are uniformly distributed on the sphere.

### 3.1.1. Isotropic Decay

Von Karman & Howarth<sup>54</sup> first suggested in 1938 that the decaying turbulence should have a power law behavior of the form:

$$K = K_0 \left( 1 + \frac{\varepsilon_0 t}{nK_0} \right)^{-n} \quad (3.1.1.1)$$

where  $K_0$  is the initial turbulent kinetic energy and  $\varepsilon_0$  represents the initial dissipation, and  $n$  is the decay exponent. While all researchers agree on the power law form, there is less agreement on what the value for  $n$  should be. However, most investigators agree that the exponent  $n$  is highly dependent on the low wavenumber  $\hat{k}$  of the energy spectrum<sup>13</sup>. In the case where the low wavenumber portion of the spectrum goes as  $\hat{k}^2$ ,  $n$  corresponds to  $3/2$  at low Reynolds number and  $6/5$  at high Reynolds number. On the other hand, when the low wavenumber portion of the spectrum goes as  $\hat{k}^4$ ,  $n$  corresponds to  $5/2$  for low Reynolds number and  $10/7$  for high Reynolds number.

We will attempt to obtain all these limits with the OEC model. For isotropic decaying turbulence, the dissipation  $\varepsilon$  is:

$$\varepsilon = -\frac{dK}{dt} \quad (3.1.1.2)$$

Substituting, equation (3.1.1.1) to (3.1.1.2) above, we obtain:

$$\varepsilon = \varepsilon_0 \left( 1 + \frac{\varepsilon_0 t}{nK_0} \right)^{-n-1} \quad (3.1.1.3)$$

In this section, our model attempts to capture the evolution of  $n$  as a function of the

turbulent Reynolds number ( $Re_T = \frac{K^2}{\nu \varepsilon}$ , with  $\nu$  being the fluid kinematic viscosity) for

both  $\hat{k}^2$  and  $\hat{k}^4$ . Figure 3 below summarizes the results obtained when the low

wavenumber behavior of the spectrum is  $\hat{k}^2$ .

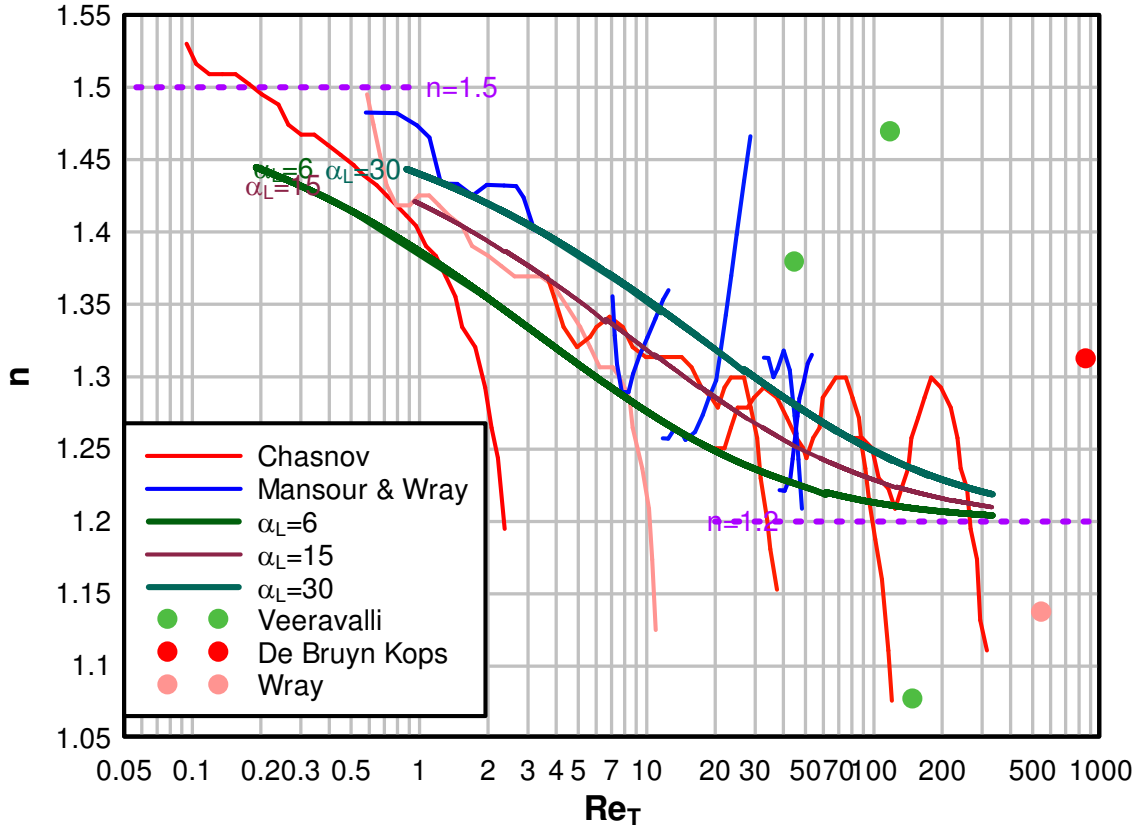


Figure 3: Power-law exponent as a function of the turbulent Reynolds number for a  $\hat{k}^2$  low wavenumber spectrum.

The thick maroon and dark green lines represent our model predictions ( $\alpha_L = 6, 15, 30$  for  $\alpha_H = 1$ ). For our purpose, we determined that the ratio  $\frac{\alpha_L}{\alpha_H} = 15$  (maroon curve) best matched the DNS simulations of Chasnov<sup>23</sup>, Mansour & Wray<sup>24</sup> and Veeravalli<sup>26</sup>. The upper and lower purple dashed lines included in the figure are the low and high Reynolds bounds on  $n$ . Notice that the model obtains these limits independent of  $\alpha_L$ . Also on Figure 3 are shown the exponent values for the DNS of de Bruyn Kops<sup>65</sup>.

When the low wavenumber behavior of the spectrum goes as  $\hat{k}^4$ , we obtained the results shown in Figure 4 below. Again, the horizontal green dash lines represent the upper (5/2) and lower (10/7) limits of the exponent for  $\hat{k}^4$  spectrum. The thick purple and blue lines are the model predictions for  $\frac{\lambda_L}{\lambda_H} = 10, 25, 50$ . In addition to these curves, there are four  $128^3$  DNS simulations by Yu et al<sup>55</sup> and four  $256^3$  DNS simulations by Mansour & Wray. For the same reason mentioned above, we determined that  $\frac{\lambda_L}{\lambda_H} = 15$  (not shown) is an adequate compromise. Note that this ratio is similar to the one determined above for  $\hat{k}^2$ .

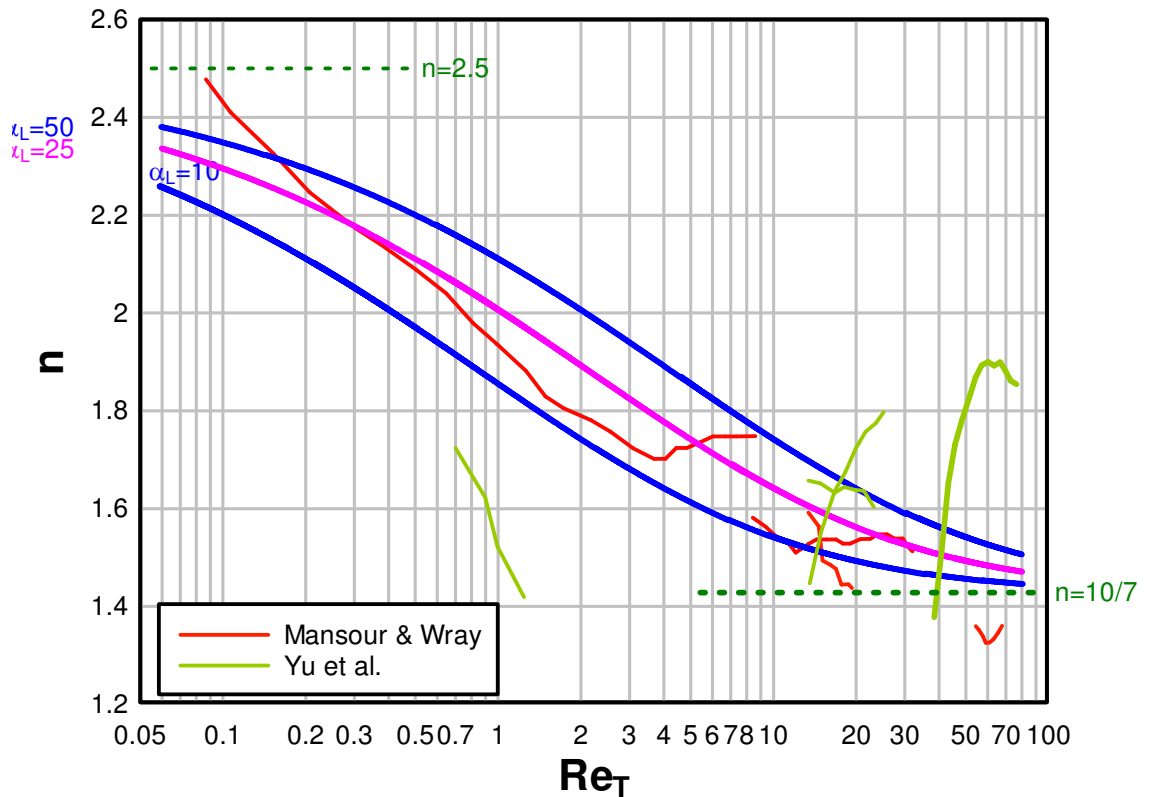


Figure 4: Power law exponent as a function of Reynolds number for a  $\hat{k}^4$  low wavenumber spectrum.

### 3.1.2. Kinetic Energy

In this section, we focus our efforts on predicting the decay of kinetic energy in isotropic flows (other than just the exponent). This is essentially a posteriori test of the chosen value  $\frac{\lambda_L}{\lambda_H} = 15$ . We test the model against numerous published data: some experimental, some LES and other DNS. In determining the kinetic energy, the equations used in our model predictions originate from equation 2.3.1 and 2.3.3 above with the particularity that the flow is isotropic. Hence, there is no need to include the return-to-isotropy (  $D_{ij} = 0$  ) as well as the diffusion terms:  $\nabla(\nu + \nu_T)\nabla\hat{R}_{ij} = 0$  ,  $\nabla(\nu + \nu_T)\nabla k_i = 0$  . Thus, in cases where no rotation is present, equations (2.3.1 and 2.3.3) become:

$$\hat{R}_{ij,t} = -\left(15\nu k^2 + \frac{1}{\tau_R}\right)\hat{R}_{ij} \quad (3.1.2.1)$$

$$k_{i,t} = -\frac{1}{l}\left(15\nu k^2 + \frac{1}{\tau_R}\right)k_i \quad (3.1.2.2)$$

where  $l = 3$  for  $k^2$  and  $l = 5$  for  $k^4$  low wave number spectra

Data and model predictions are shown below for low and intermediate turbulent Reynolds numbers. In addition, we state all initial conditions in Table 2 below:

	<b>Wigeland &amp; Nagib<sup>63</sup></b> (exp. Data)			<b>Mansour, Cambon &amp; Speziale<sup>62</sup></b> (DNS)		<b>Jacquin<sup>61</sup></b> (exp. Data)			<b>de Bruyn Kops &amp; Riley<sup>20</sup></b> (DNS)	<b>Squires<sup>60</sup></b> (LES)	
$\epsilon(\text{m}^2/\text{s}^3)$	14.85	2.96	2.77	0.93	0.95	11.73	16.43	30.93	0.782	1.27	1.35
$K(\text{m}^2/\text{s}^2)$	0.098	0.045	0.029	0.964	0.977	0.15	0.264	0.462	0.087	0.265	0.298
$v(\text{m}^2/\text{s})$	1.8	1.8	1.8	3.67	1.49	1.51	1.51	1.51	1.49	8.6	8.6
	e-5	e-5	e-5	e-2	e-2	e-5	e-5	e-5	e-5	e-5	e-5
$Re_T$	36	38	17	27.2	67.1	127	281	457	655	643	764

Table 2: Initial Conditions

In Figure 5, the kinetic energy is represented versus time. The asterisks, the triangles and the stars correspond to the experimental data with corresponding  $Re_T=36$ , 38 and 17 while the dashed lines correspond to our simulations.

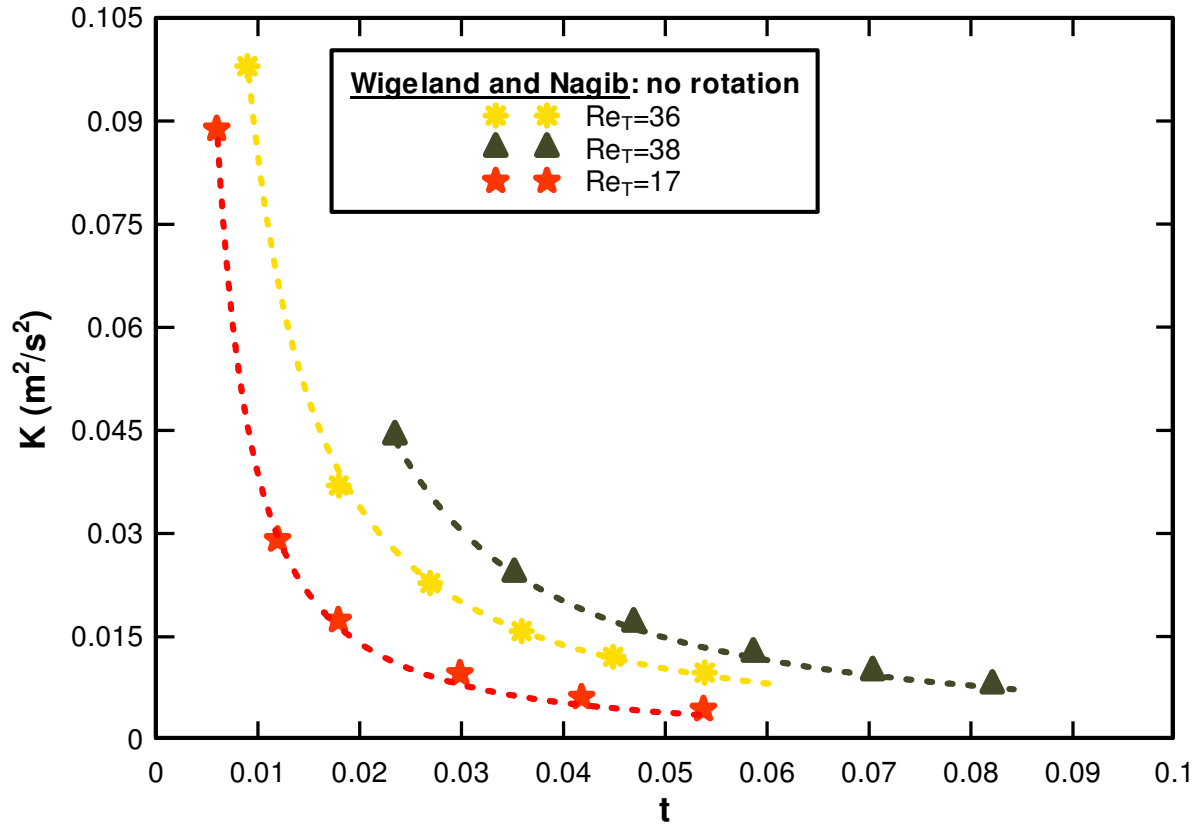


Figure 5: Wigeland and Nagib's decaying kinetic energy.

In Figure 6, the kinetic energy versus time is shown. The orange dots correspond to the experimental data for  $Re_T=27.24$  and the purple ones are for  $Re_T=67.1$ . The solid lines correspond to our simulations. Clearly, the OEC model shows good agreement with the DNS data of Mansour, Cambon and Speziale<sup>62</sup>.

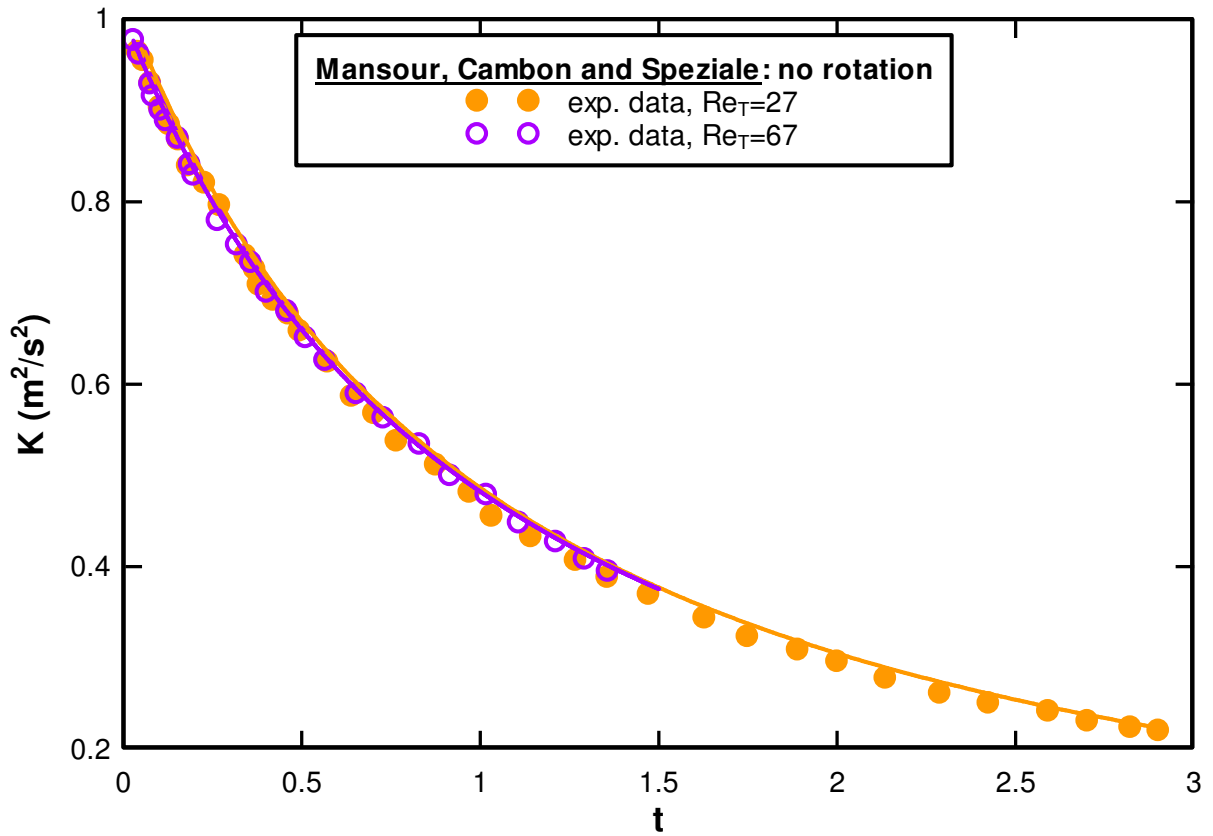


Figure 6: Mansour, Cambon and Speziale's decaying kinetic energy.

Figure 7 shows the kinetic energy versus time. The asterisks correspond to the experimental data and the dashed lines correspond to the simulations.

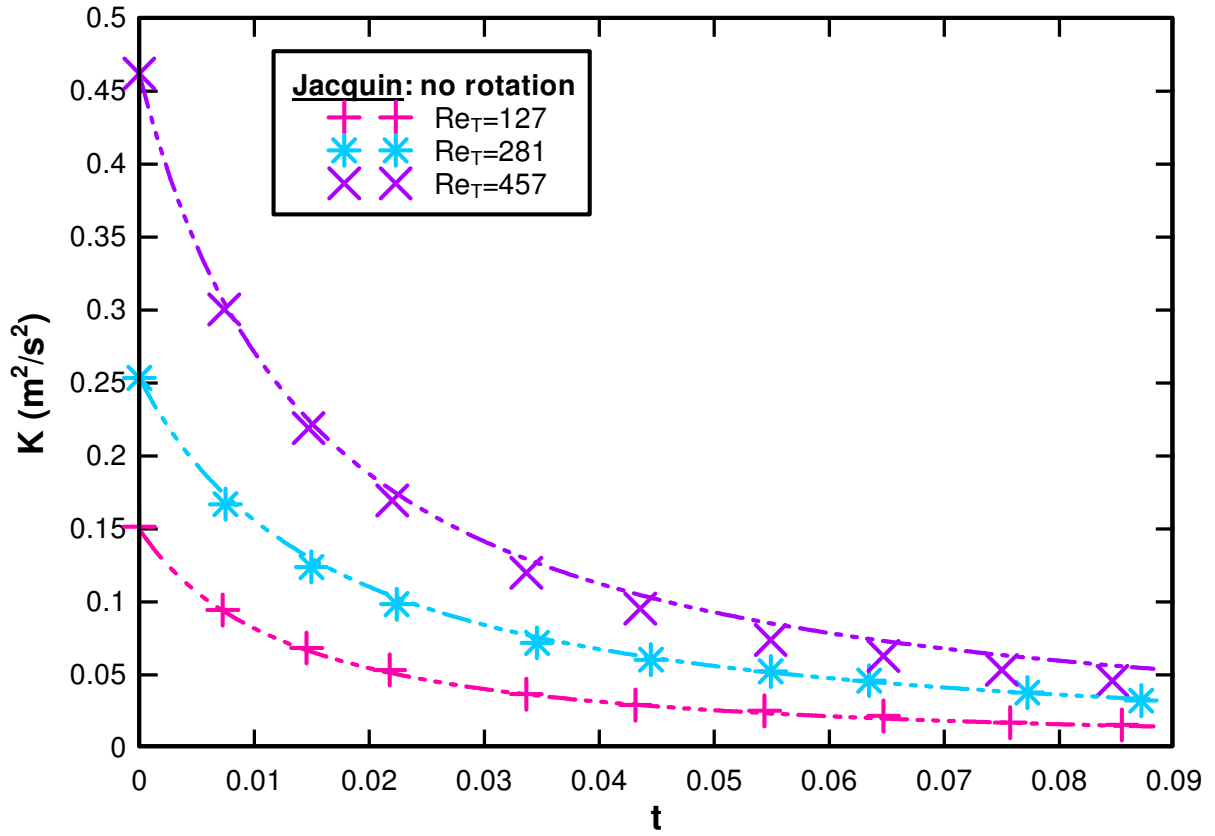


Figure 7: Jacquin's decaying kinetic energy.

Figure 8 shows the kinetic energy versus time. The red asterisks correspond to DNS data of de Bruyn Kops & Riley<sup>20</sup> for  $Re_T=655$  and the dashed lines correspond to the oriented eddy model simulations.

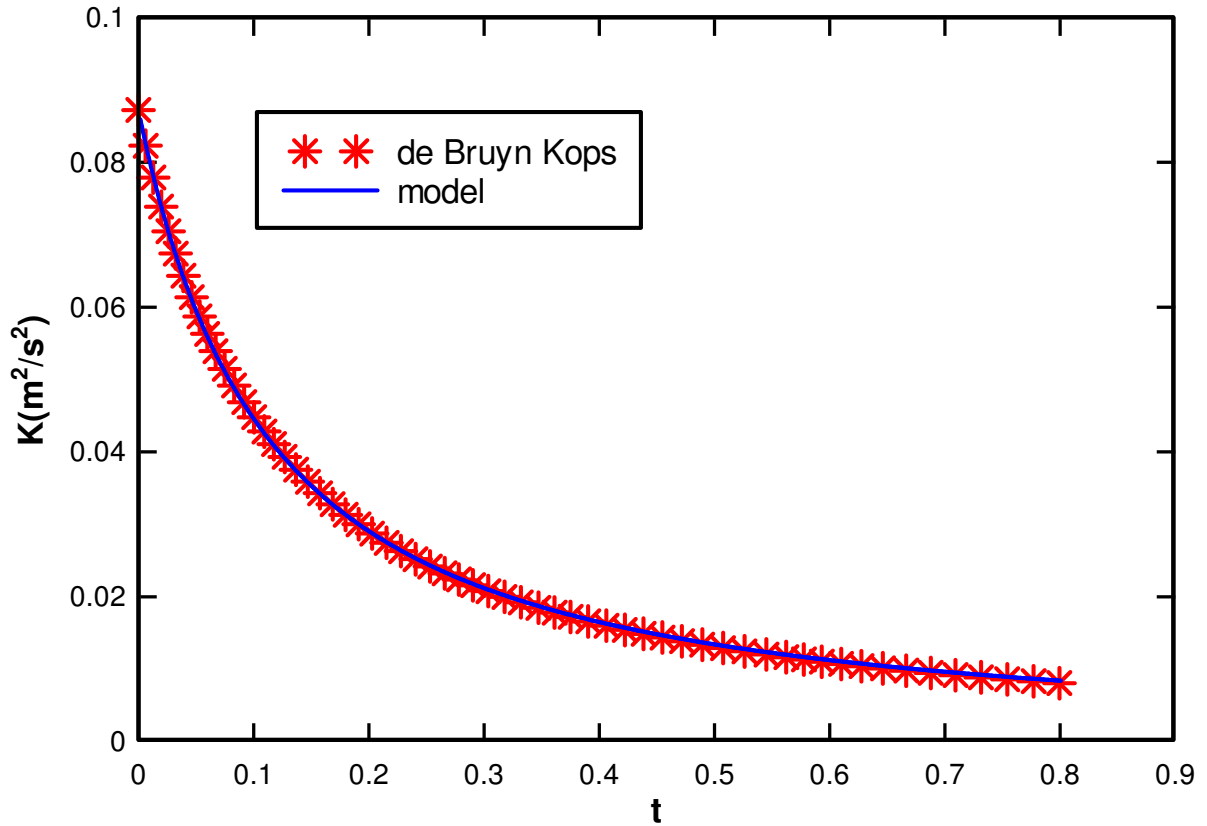


Figure 8: de Bruyn Kops & Riley's decaying kinetic energy.

Figure 9 shows the kinetic energy versus time. The green asterisks correspond to the  $\hat{k}^2$  experimental data with  $Re_T = 643$ . The red asterisks represent  $\hat{k}^4$  data with  $Re_T = 764$ . The blue and pink lines correspond to our simulations.

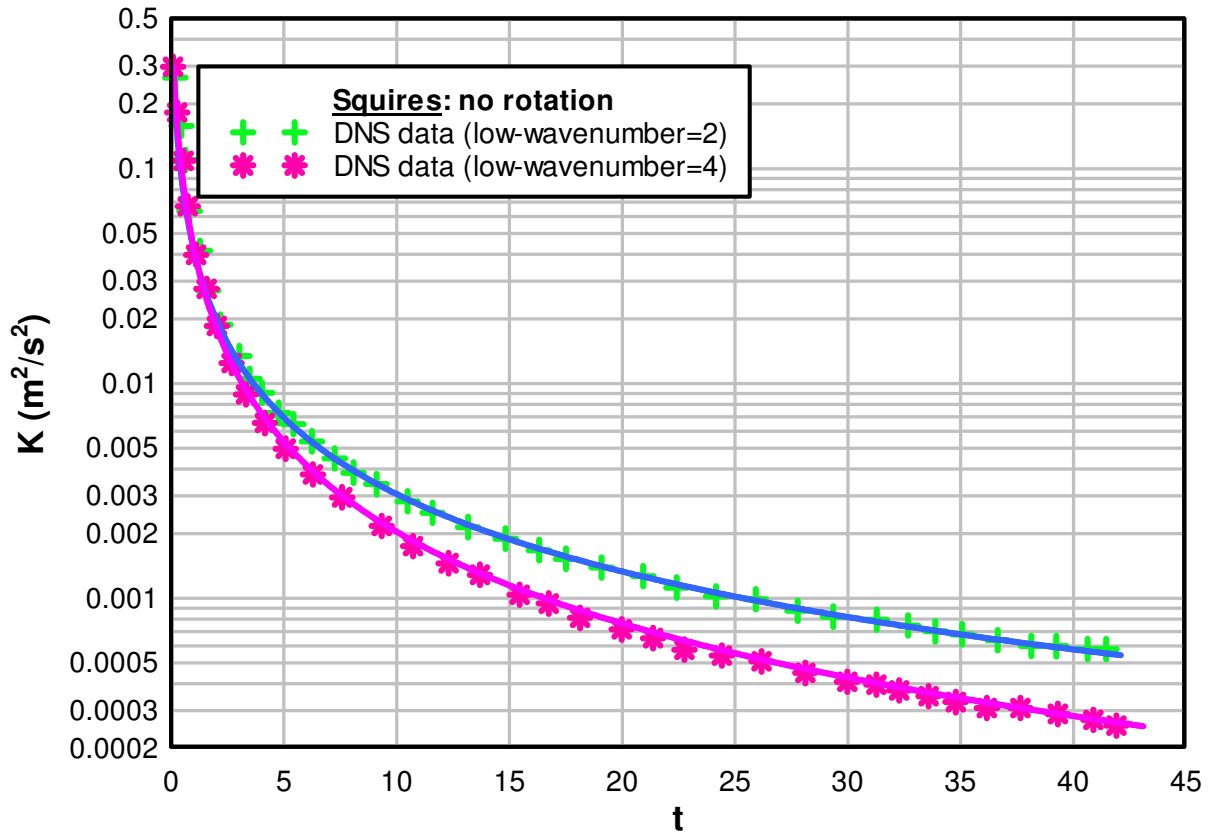


Figure 9: Squires' decaying kinetic energy for both  $\hat{k}^2$  and  $\hat{k}^4$ .

Based on the data presented above, it is concluded that the OEC model performs well in predicting the decaying kinetic energy for simple (homogeneous, isotropic and irrotational) turbulent flows.

### 3.1.3. Rotating Decaying Grid-Turbulence

To measure the degree of rotation present in the flow, we used the turbulent Rossby number defined as follow:

$$Ro_T = \frac{\varepsilon}{K\Omega^*} \quad (3.1.3.1)$$

Large  $Ro_T$  means no rotation, whereas  $Ro_T < 1$  implies a flow dominated by rotation.

With rotation present, the model equations become:

$$k_{i,t} = -\frac{1}{3}(15\nu k^2 + \frac{1}{\tau_R})k_i - \frac{1}{\tau_R}n_i \quad (3.1.3.2)$$

Three models for the rotation term were tested:

$$n_i^A = \frac{|\vec{k} \cdot \vec{\Omega}^*|}{(C_1 k^2 K^{\frac{1}{2}} + C_2 |k| \Omega^*)} k_i$$

or

with  $n_i^B = \frac{(\vec{k} \cdot \vec{\Omega}^*)}{(C_1 k^2 K + C_2 (\vec{\Omega}^*)^2)} \Omega_i^*$  (3.1.3.3)

or

$$n_i^C = \frac{(\vec{k} \cdot \vec{\Omega}^*)^2 / k^2}{(C_1 k^2 K + C_2 (\vec{\Omega}^*)^2)} k_i$$

where  $\Omega_i^* = \varepsilon_{ijk} U_{k,j} + \Omega_i^{\text{frame}}$ . In our earlier work, (*Eddy Collision Models for Turbulenc*<sup>64</sup>), Chartrand briefly looked at the first two models,  $n_i^A$  and  $n_i^B$ . However, after extensively studying the performance of each of these models and comparing them to multiple DNS results, we came to the conclusion that the above two terms each only captures a different aspect of the rotation. Hence, the third model was developed.

With each model, come two constants  $C_1$  and  $C_2$  that are used to tune the model behavior. That is,  $C_1$  and  $C_2$  are both model-dependent. From equations (3.1.3.3) above,

it is clear that  $C_2$  affects simulations at large rotation rates while  $C_1$  acts at small rotation rates. We used this concept in determining the values for both  $C_1$  and  $C_2$ . Table 3 below summarizes the values:

Model	Formula	$C_1$	$C_2$
k	$\frac{ \vec{k} \cdot \vec{\Omega}^* }{(C_1 k^2 K^{\frac{1}{2}} + C_2  k   \Omega^* )} k_i$	8	0.25
$\Omega$	$\frac{(\vec{k} \cdot \vec{\Omega}^*)}{(C_1 k^2 K + C_2 (\vec{\Omega}^*)^2)} \Omega_i^*$	20	1/4
Smooth k	$\frac{(\vec{k} \cdot \vec{\Omega}^*)^2 / k^2}{(C_1 k^2 K + C_2 (\vec{\Omega}^*)^2)} k_i$	20	1/4

Table 3: Rotation-models along with their respective tuning constants  $C_1$  and  $C_2$

Next, we compared the performance of each model for three sets of data: Jacquin<sup>61</sup>, ManCamSpe (Mansour, Cambon & Speziale<sup>62</sup>) and Blaisdell<sup>7</sup>. The *k-smooth* model outperforms the other two. The initial conditions are shown in Tables 4, 5 and 6 below:

	Mansour, Cambon & Speziale <sup>62</sup>				Jacquin <sup>61</sup>			Blaisdell <sup>7</sup>
$\epsilon(\text{m}^2/\text{s}^3)$	0.93		0.95		11.73	16.43	30.93	1.78
$K(\text{m}^2/\text{s}^2)$	0.964		0.977		0.153	0.288	0.444	1
$v(\text{m}^2/\text{s})$	3.67e-2		1.49e-2		1.51e-5	1.51e-5	1.51e-5	4.41e-2
$Re_T$	27.2		67.1		127	281	457	12.75
$Ro_T$	0.37	0.037	0.24	0.1	1.22	0.91	1.10	---
<b>S</b>	---	---	---	---	---	---	---	3

Table 4: Initial conditions of Mansour, Cambon & Speziale, Jacquin and Blaisdell.

	<b>Wigeland &amp; Nagib<sup>63</sup></b>					
$\epsilon(\text{m}^2/\text{s}^3)$	14.67	14.94	3.49	3.36	3.36	22.26
$\mathbf{K}(\text{m}^2/\text{s}^2)$	0.0975	0.105	0.0462	0.051	0.033	0.096
$\mathbf{v}(\text{m}^2/\text{s})$	1.8e-5	1.8e-5	1.8e-5	1.8e-5	1.8e-5	1.8e-5
$\mathbf{Re}_T$	36	41	34	43	18	23
$\mathbf{Ro}_T$	7.52	1.78	3.77	0.82	5.09	2.9

Table 5: Wigeland & Nagib's initial conditions.

	<b>Shimomura<sup>66</sup></b>			<b>de Bruyn Kops<sup>65</sup></b>	<b>Veeravalli<sup>26</sup></b>	
$\epsilon(\text{m}^2/\text{s}^3)$	0.024	0.025	0.028	0.0992	7.96	8.13
$\mathbf{K}(\text{m}^2/\text{s}^2)$	0.098	0.2619	0.5638	5.888e-2	0.17	0.202
$\mathbf{v}(\text{m}^2/\text{s})$	8.0e-3	8.0e-3	8.0e-3	1.4854e-5	1.6e-5	1.6e-5
$\mathbf{Re}_T$	50	343	1419	2353	227	313
$\mathbf{Ro}_T$	N/A	0.095	0.017	0.006	0.5	0.32

Table 6: Initial conditions of Shimomura, de Bruyn Kops and Veeravalli.

In Figure 10 below, the performance of each model is analyzed using the DNS data from Jacquin<sup>61</sup>. Our simulation matched the dimensionless initial conditions of Jacquin<sup>61</sup> as represented in Table 4. The crosses, stars and dots represent the experimental data. The solid lines represent  $\omega$ , the dashed lines  $k$  and the dotted lines  $k$ -smooth.

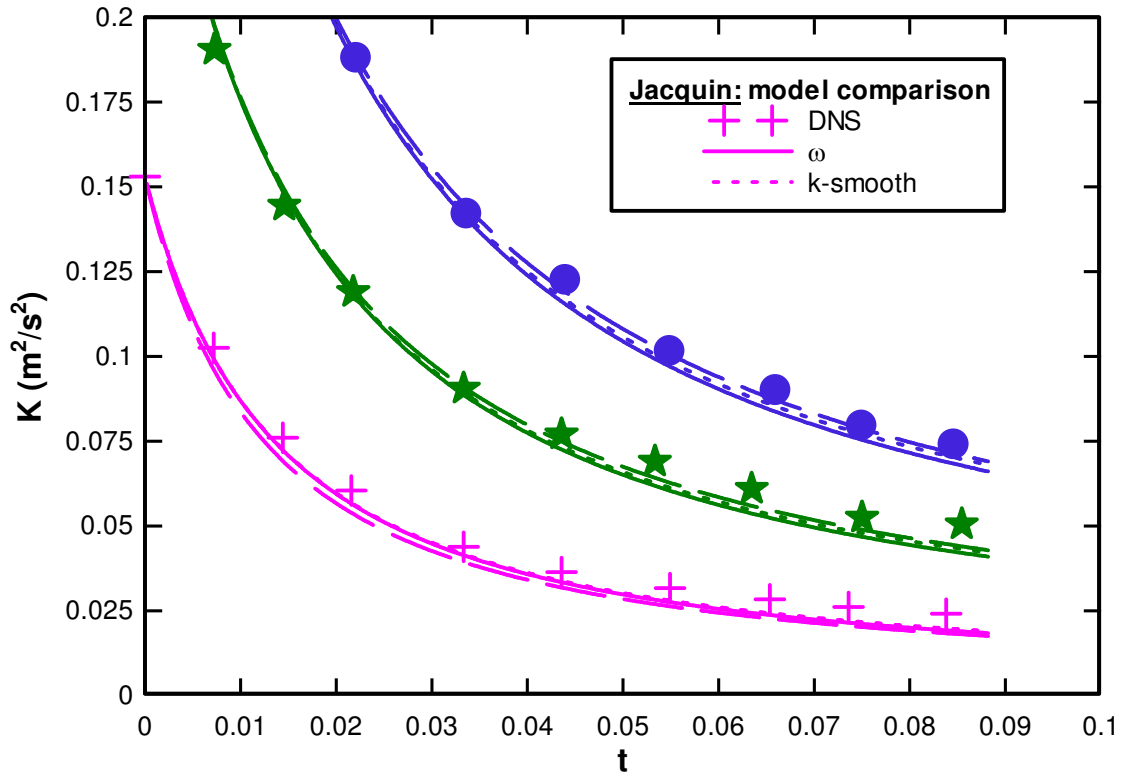


Figure 10: Performance comparison of  $k$ ,  $\omega$  and  $k$ -smooth rotation terms.

Looking at the graph above, it is concluded that all three rotation models performed equally in this case, due to the somewhat identical turbulent Rossby numbers (1.22, 0.91 and 1.10).

In Figure 11, the dimensionless initial conditions of Mansour, Cambon & Speziale<sup>62</sup> were matched for  $Re_T=27.24$ .

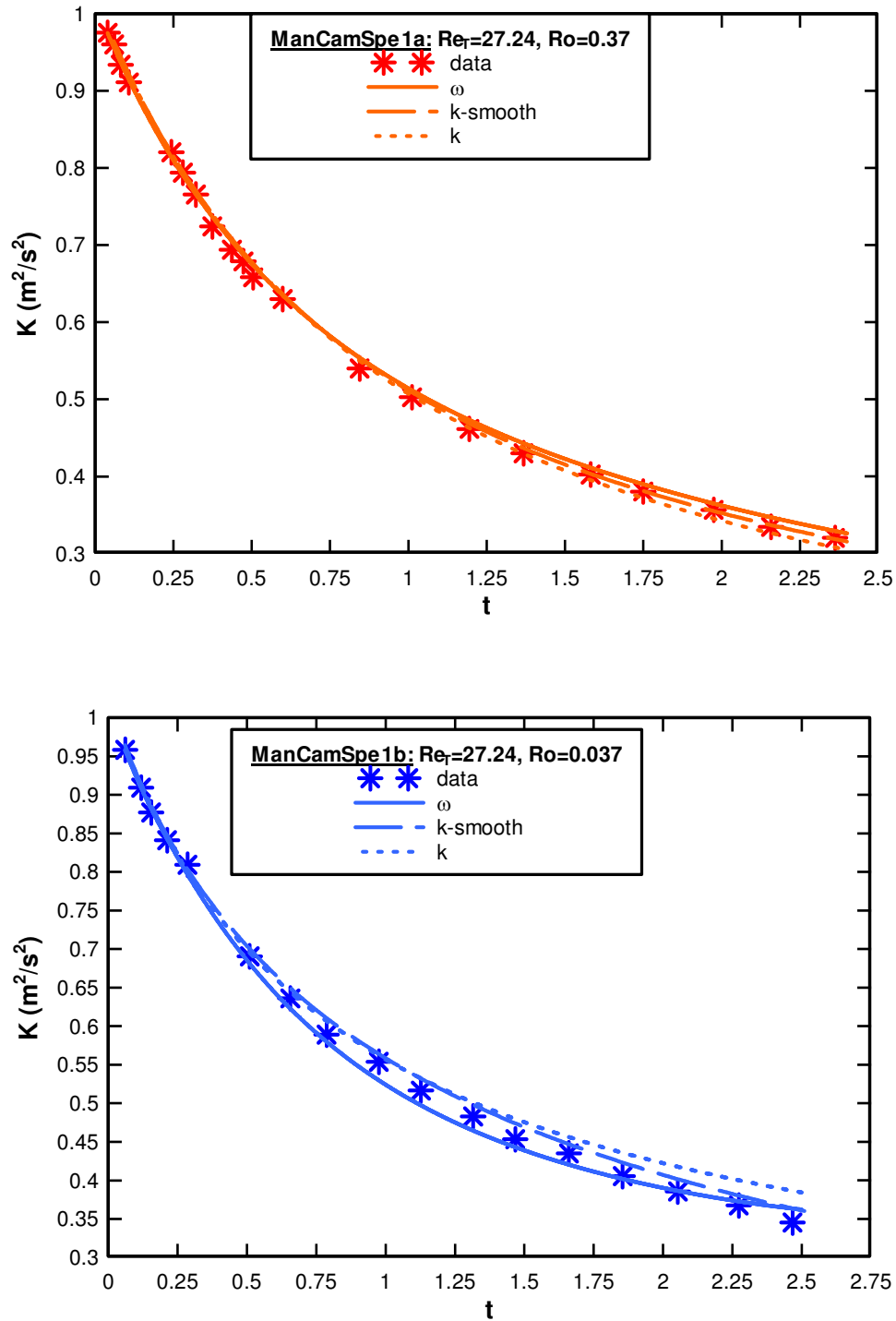


Figure 11: Performance comparison of  $k$ ,  $\omega$  and  $k$ -smooth rotation terms based on Mansour, Cambon and Speziale experimental data. a)  $Ro=0.37$ . b)  $Ro=0.037$ .

In Figure 12, the dimensionless initial conditions of Mansour, Cambon & Speziale<sup>62</sup> were matched for  $Re_T=67.1$ .

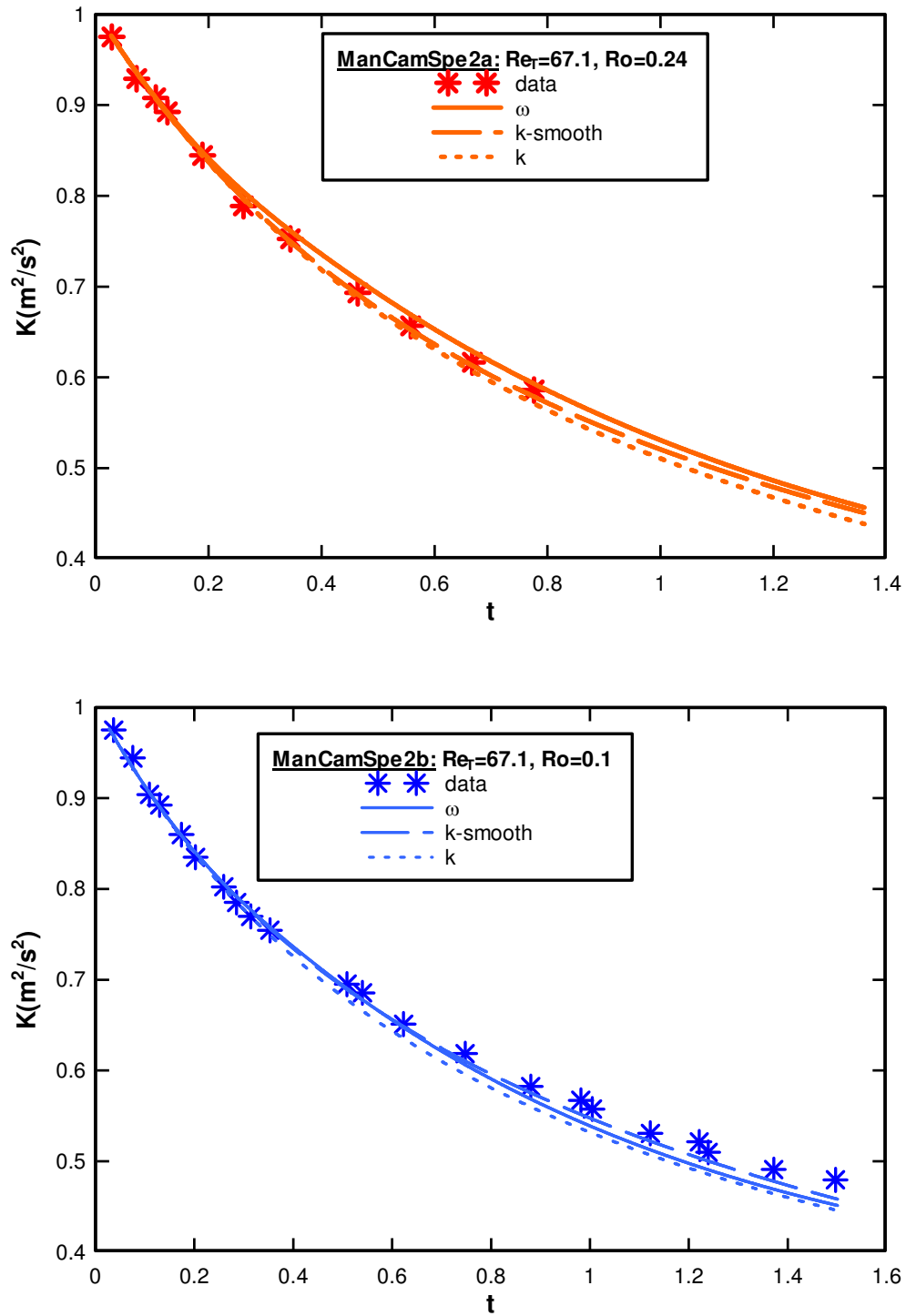


Figure 12: Performance comparison of  $k$ ,  $\omega$  and  $k$ -smooth rotation terms based on Mansour, Cambon and Speziale's experimental data. a)  $Ro=0.24$ . b)  $Ro=0.1$ .

We also evaluated all three rotational models for homogeneous flows; specifically, using data from Blaisdell's elliptical flow as shown below in Figure 13:

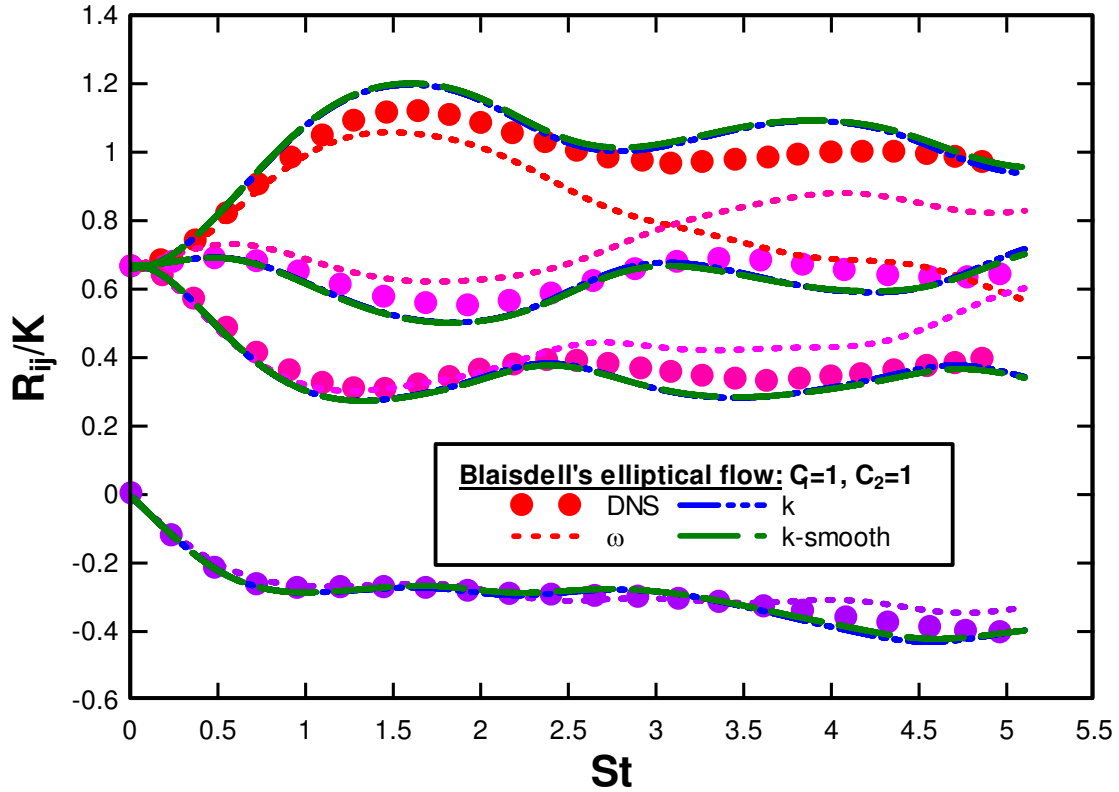


Figure 13: Performance comparison of  $k$ ,  $\omega$  and  $k$ -smooth rotation terms for Blaisdell<sup>7</sup>.  
(homogeneous shear flow)

From the graphs above, the  $k$ -smooth model is always consistently between the  $k$  and the  $\omega$ -models. And sometimes the difference is so subtle that it is almost negligible. In the Blaisdell<sup>7</sup> case however, the  $\omega$ -model performs very poorly. Hence, it was decided that the  $k$ -smooth model performs the best. So, the OEC model was tested against other published data such as Wigeland & Nagib<sup>63</sup>, Jacquin<sup>61</sup>, Shimomura<sup>66</sup>, de Bruyn Kops<sup>65</sup>, Veeravalli<sup>26</sup> and Mansour, Cambon & Speziale<sup>62</sup>. (The initial conditions are presented in

Tables 5 and 6 above). The rotating initial conditions for Wigeland & Nagib as well as de Bruyn Kops were already given above in section 3.1.3.

In Figure 14 below, the asterisks, triangles and stars represent the experimental data of Wigeland & Nagib<sup>63</sup> for low Reynolds number, while the dotted lines represent the predictions for the collision model.

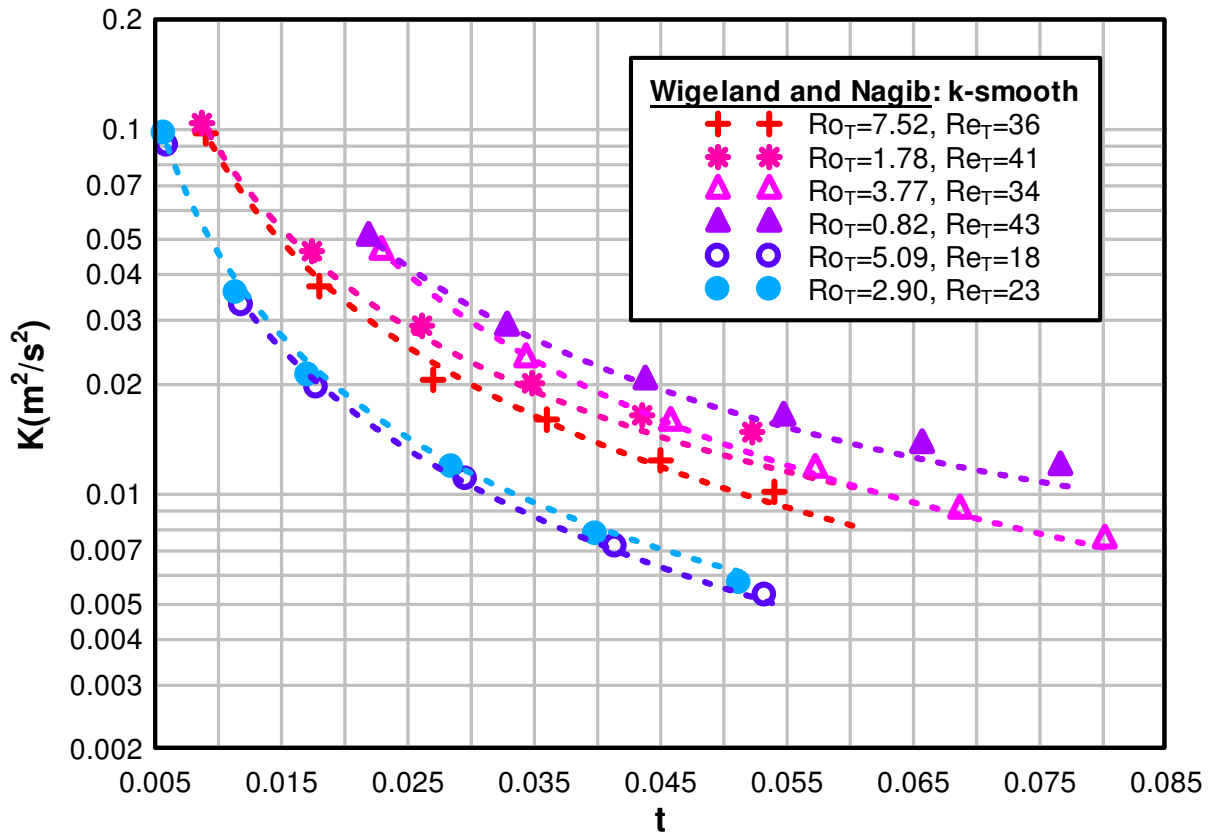


Figure 14: Rotating isotropic decay of Wigeland & Nagib using the rotation model  $n_i^C$ . Turbulent kinetic energy versus time.

In Figure 15, the asterisks, crosses and squares represent the experimental data of Jacquin<sup>61</sup>, while the dashed lines represent the predictions of the collision model with  $n_i^C$  for rotation model. The numbers 140, 310 and 500 correspond to the turbulent Reynolds number:

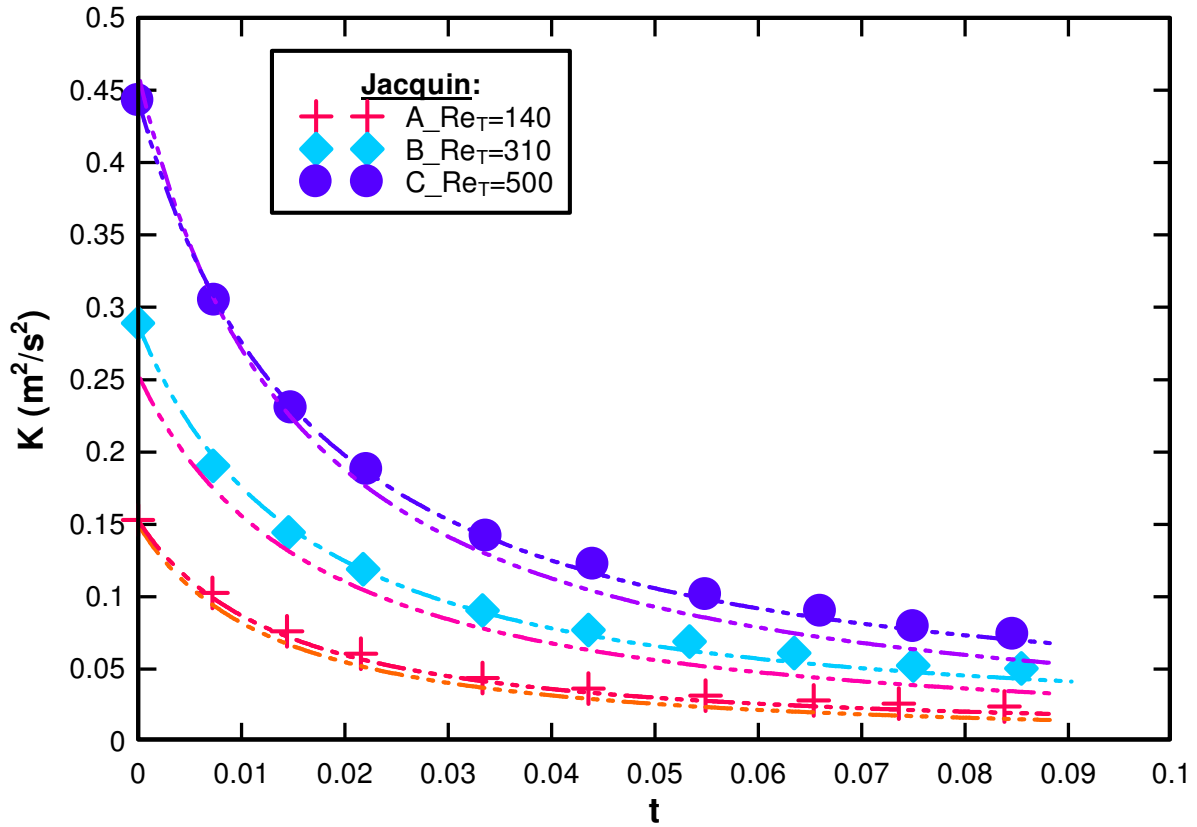


Figure 15: Rotating Isotropic decay of Jacquin. Turbulent kinetic energy versus time.

In Figure 16, the asterisks represent the experimental data of Shimomura<sup>66</sup> (for both irrotational and rotational cases), while the solid lines represent the predictions from our

collision model. As summarized in Table 6 above, the turbulent Reynolds numbers correspond respectively to 50, 343 and 1419. In addition, the data sets are for  $\hat{k}^2$ .

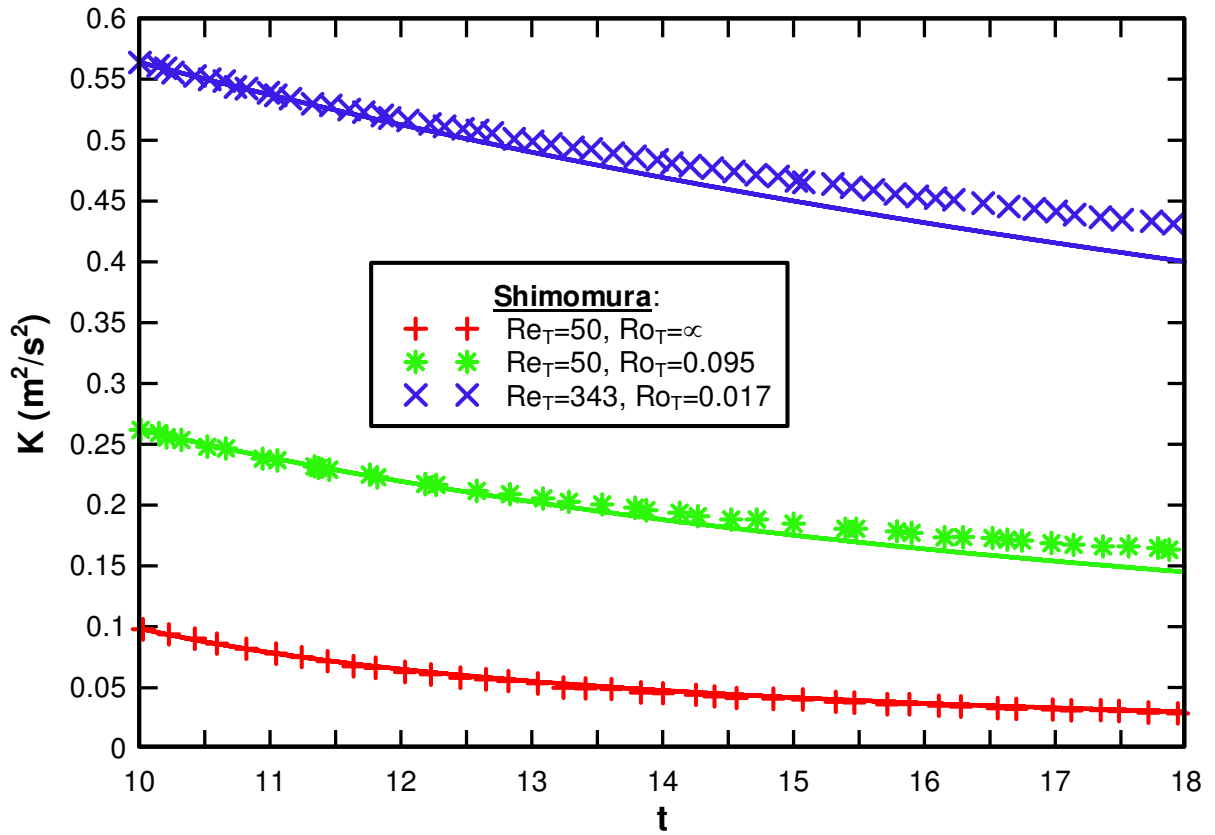


Figure 16: Rotating isotropic decay of Shimomura. Turbulent kinetic energy versus time.

In Figures 17 and 18, the asterisks represent the experimental data and the solid lines represent the predictions from our collision model.

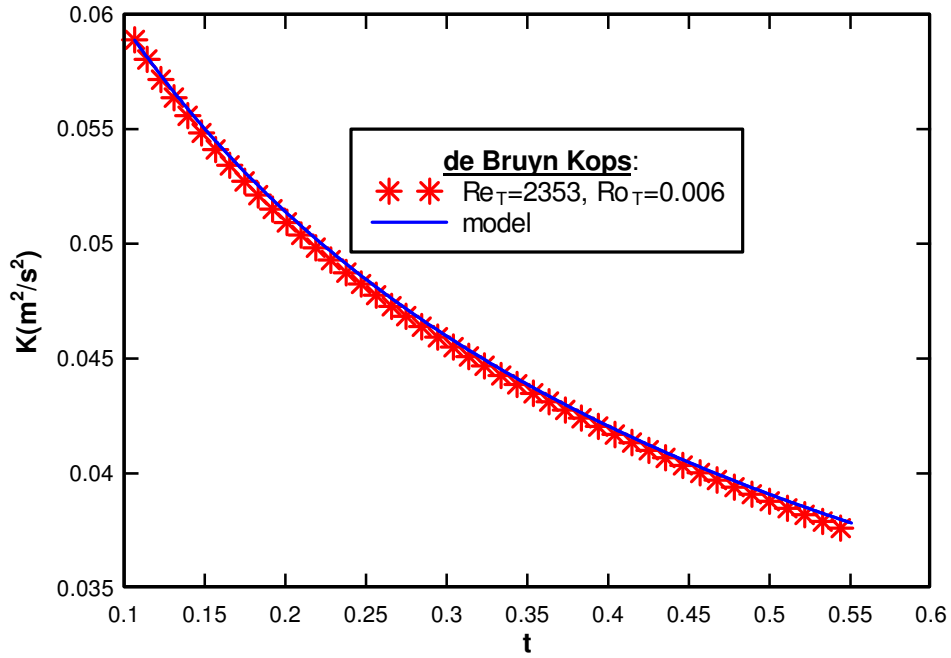


Figure 17: de Bruyn Kops<sup>65</sup> rotating decaying turbulence. Turbulent kinetic energy versus time.

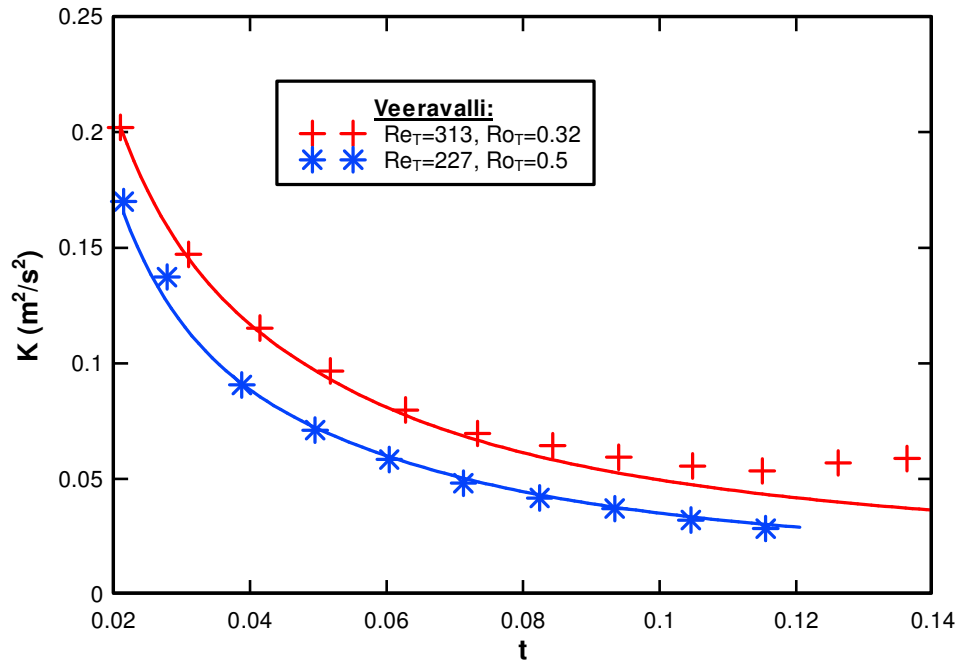


Figure 18: Veeravalli<sup>26</sup>'s decaying kinetic energy. Kinetic energy versus time.

In Figure 19, the asterisks represent the experimental data and the solid lines represent the predictions from the OEC model.

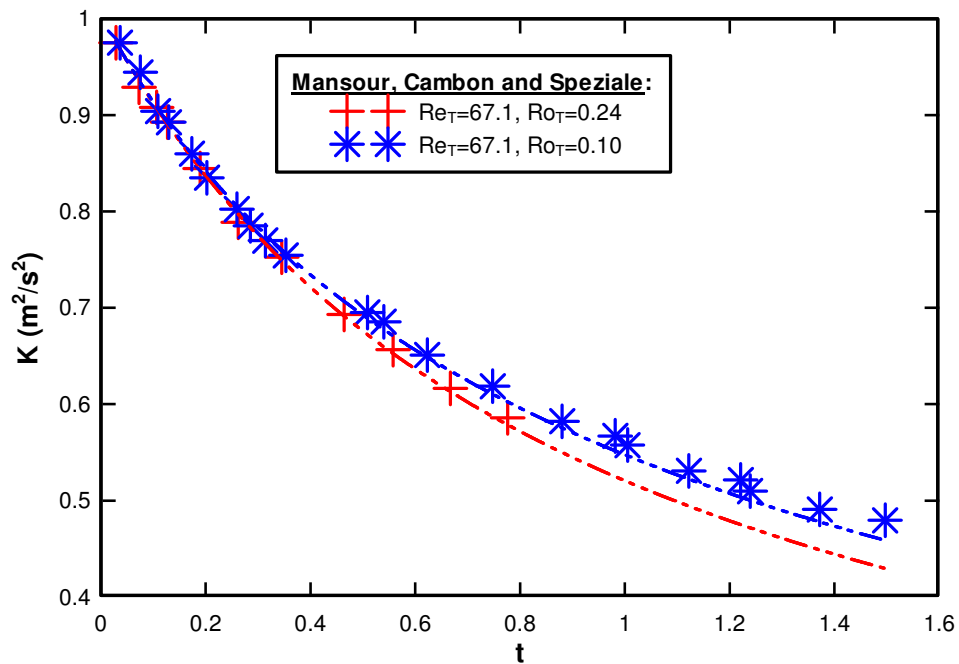
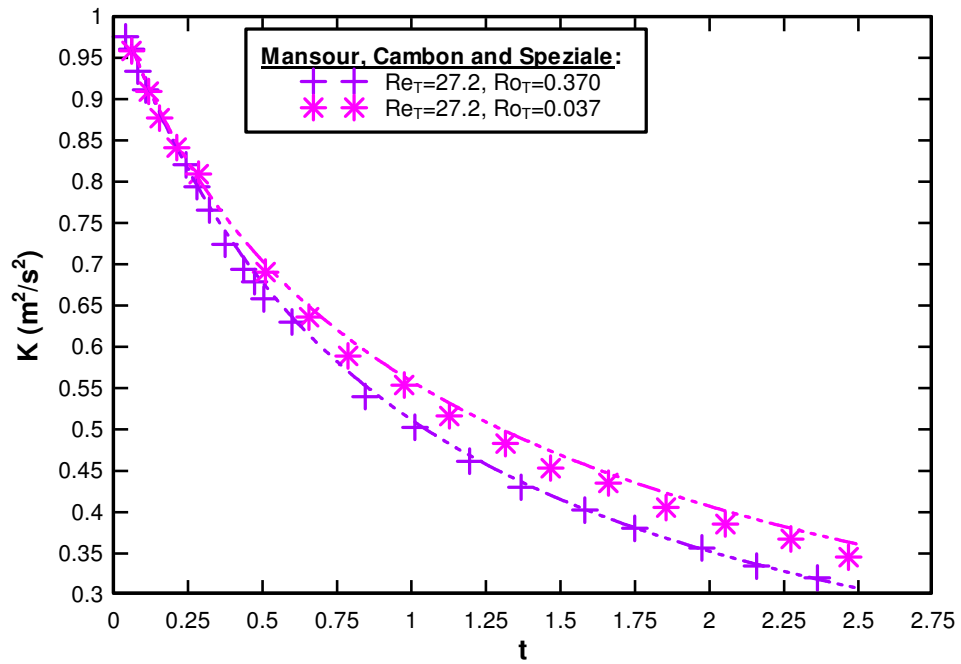


Figure 19: Rotating isotropic decay of Mansour, Cambon and Speziale. Turbulent kinetic energy versus time. a)  $Re_T=27.2$  and b)  $Re_T=67.1$

### 3.2. Rapid Distortion Theory

In turbulent shear flows, the turbulence-to-mean-shear time scale ratio defined as  $SK/\varepsilon$  varies between 0 and  $\infty$ . In the limiting cases when the ration  $SK/\varepsilon$  is exceptionally large, the evolution of the turbulence is then described exactly by rapid-distortion theory or RDT. Previous work compared this model performance to that of a standard RDT solver (by Chartrand<sup>64</sup>). This time, we compare our model performance to that of RDT cases of Matsumoto<sup>16</sup>, Blaisdell<sup>7</sup> and Lee & Reynolds<sup>15</sup>, with initial conditions summarized in Table7 below. Lee & Reynolds experimented three cases: axisymmetric contraction (AC), axisymmetric expansion (AE) and plane strain (PS). Matsumoto's case includes two DNS (high and low Reynolds numbers) with shear (S) deformation while Blaisdell has one elliptical (E) case.

	Lee & Reynolds <sup>15</sup>			Matsumoto <sup>16</sup>	Blaisdell <sup>7</sup>
	(AC)	(AE)	(PS)	(S)	(E)
$\varepsilon(\text{m}^2/\text{s}^3)$	0.018	0.122	0.25	0.185	1.79
$\mathbf{K}(\text{m}^2/\text{s}^2)$	1.0	1.0	1.0	0.2	1
$\mathbf{v}(\text{m}^2/\text{s})$	10	10	10	1.2e-2	4.41e-2
$\mathbf{S}(\text{s}^{-1})$	1	0.5	1.0	28.28	3.0
$\mathbf{Re}_T$	5.59	0.82	0.4	18.18	12.75
$\mathbf{SK}/\varepsilon$	55.87	4.08	4	30.6	1.68

Table 7: Initial conditions of Matsumoto, Lee & Reynolds and Blaisdell.

Also, included in Table 8 are the non-zero mean velocity gradients for simple deformations:

	Axisymmetric contraction	Axisymmetric expansion	Plane Strain	Shear
$R_{11}$	$S$	$-2S$	$S$	$0$
$R_{22}$	$-\frac{1}{2}S$	$S$	$-S$	$0$
$R_{33}$	$-\frac{1}{2}S$	$S$	$0$	$0$
$R_{12}$	$0$	$0$	$0$	$S$
$S \equiv (2\bar{S}_{ij}\bar{S}_{ij})^{1/2}$	$\sqrt{3}S$	$2\sqrt{3}S$	$-2S$	$2S$

Table 8: Tensor matrix for simple deformations.

The graphs below summarize our results:

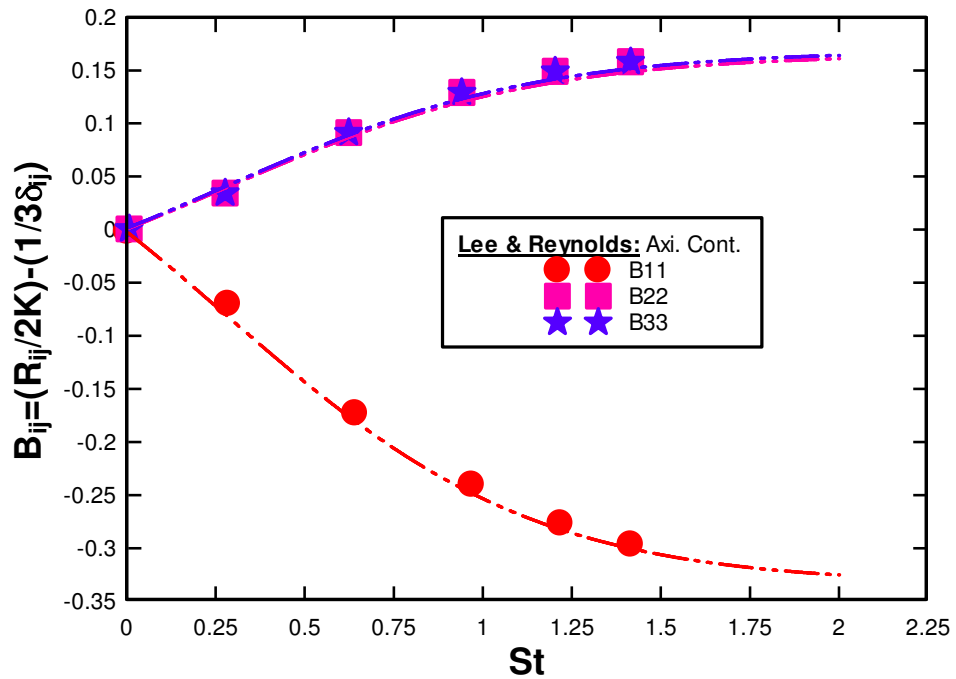


Figure 20: Lee & Reynolds' axisymmetric contraction. The dots represent the DNS and the lines represent the OEC model prediction.  $SK/\varepsilon=55.9$ .

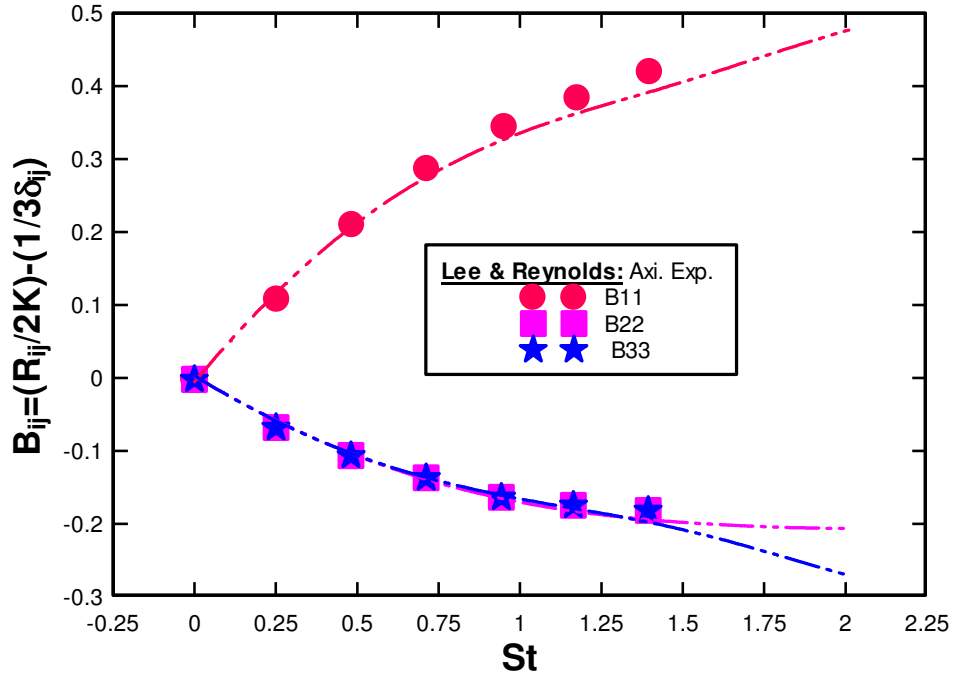


Figure 21: Lee & Reynolds' axisymmetric expansion. The dots represent the DNS and the lines represent the OEC model prediction.  $SK/\varepsilon=5.08$ .

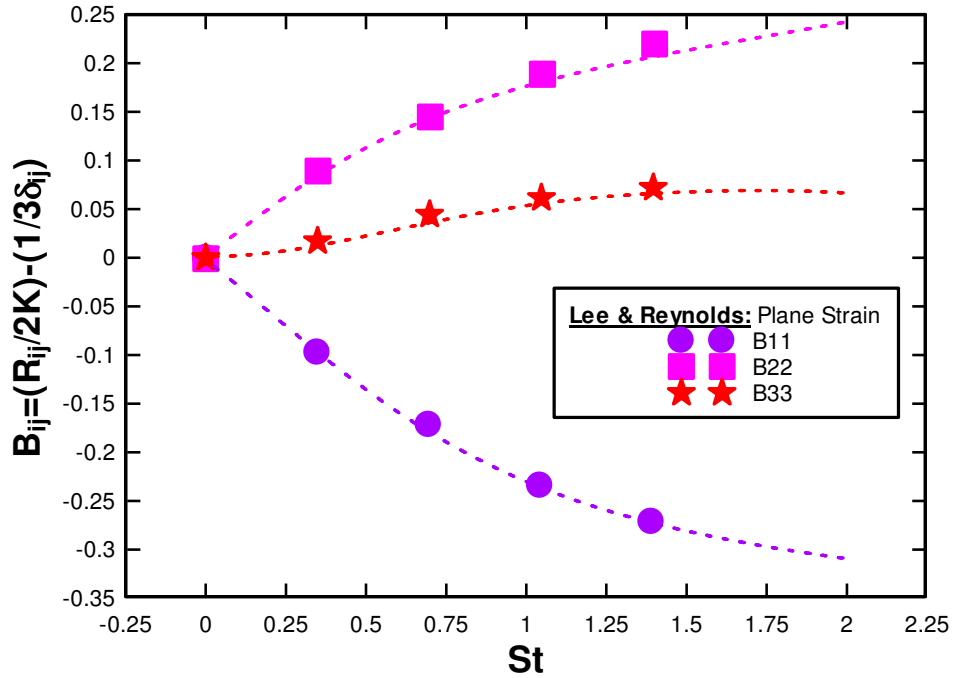


Figure 22: Lee & Reynolds' plane strain. The dots represent the DNS and the lines represent the OEC model prediction.  $SK/\varepsilon=4$ .

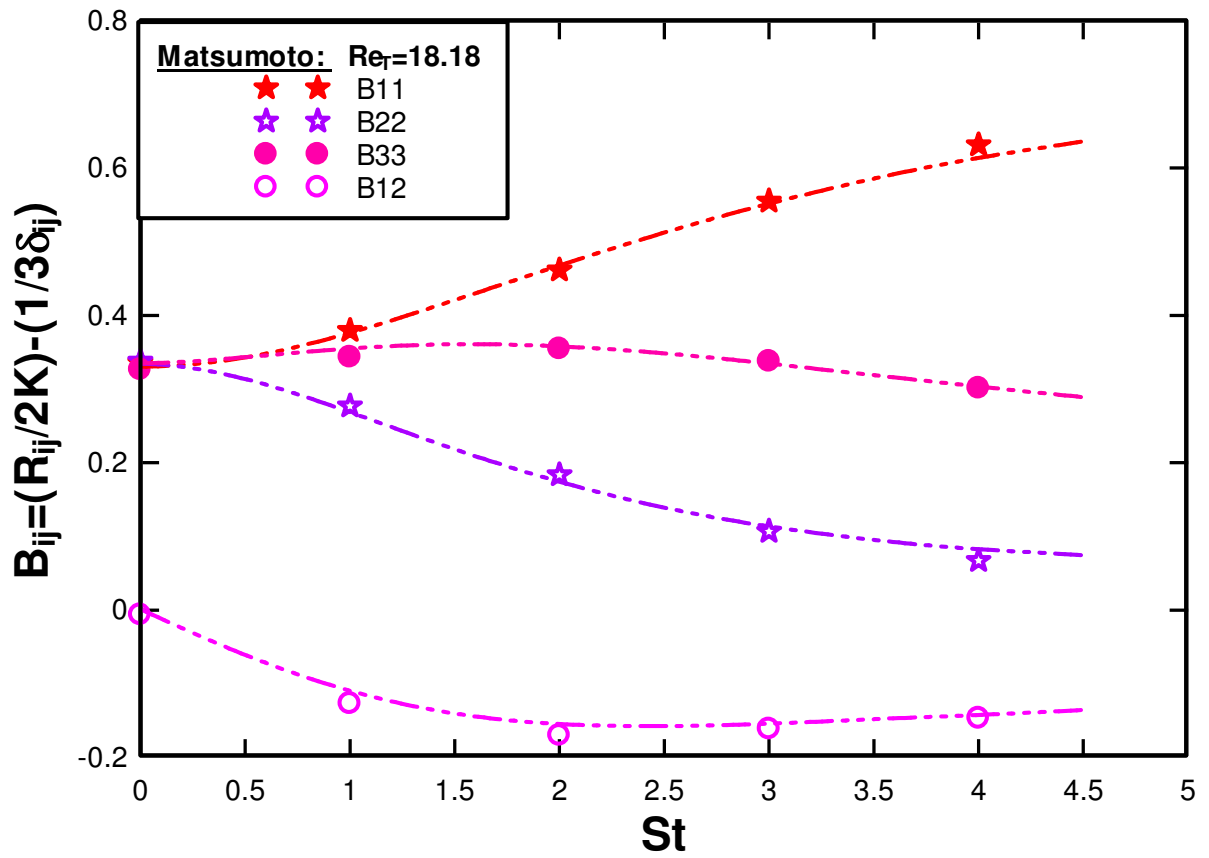


Figure 23: Matsumoto's shear deformation. The dots represent the DNS data and the lines represent the OEC model prediction. The large imposed strain ( $SK/\varepsilon=30.6$ ) implies RDT is closely approximated.

The next simulation we did is based on Blaisdell<sup>7</sup>'s DNS. Here, the fact that both the strain ratio and the turbulent Reynolds number are small (respectively 1.68 and 12.75) in addition to the initial random field justifies the RDT approximation. Furthermore, we ran four simulations: one with only the return-model on, a second one with just the rotation model on, a third one with both return and rotation models on, and finally the RDT case (return and rotation models both turned off). Looking at the graph below, we were able to prove that both return and rotation have no effects in this case. The results are shown below in Figure 24 and 25. The dots represent the DNS and the lines show the model prediction.

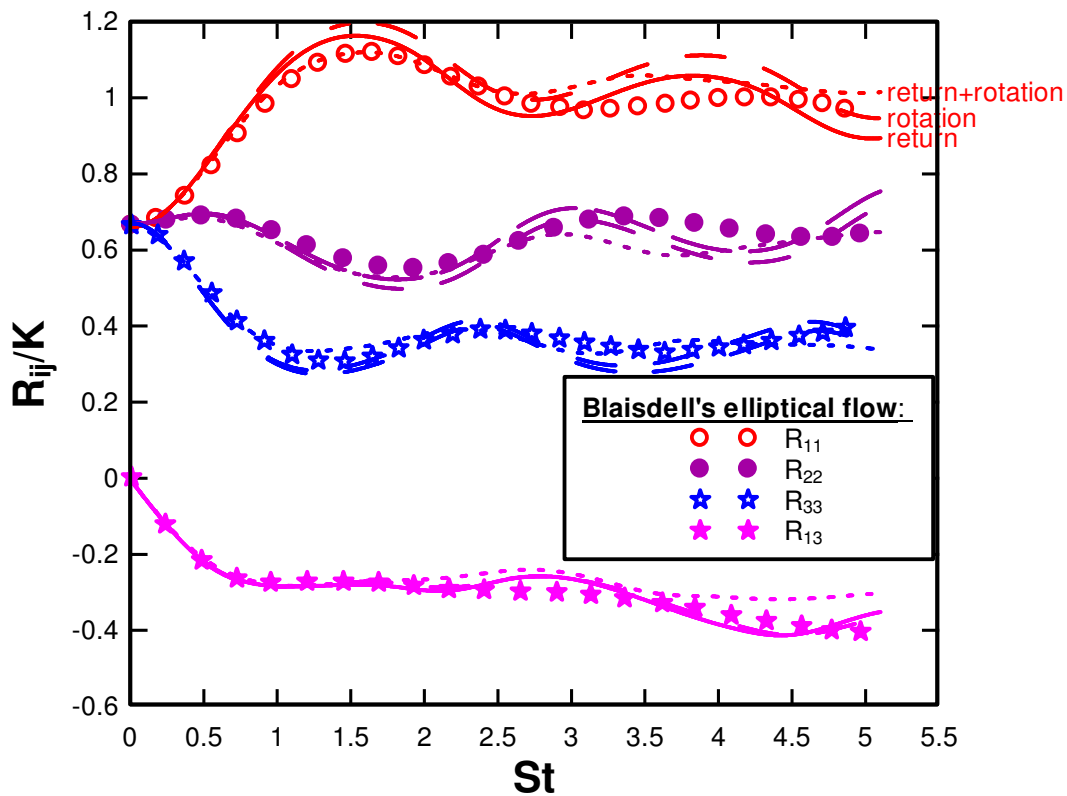


Figure 24: Blaisdell's elliptical flow with a) return model on, b) rotation model on and c) both return and rotation models on.

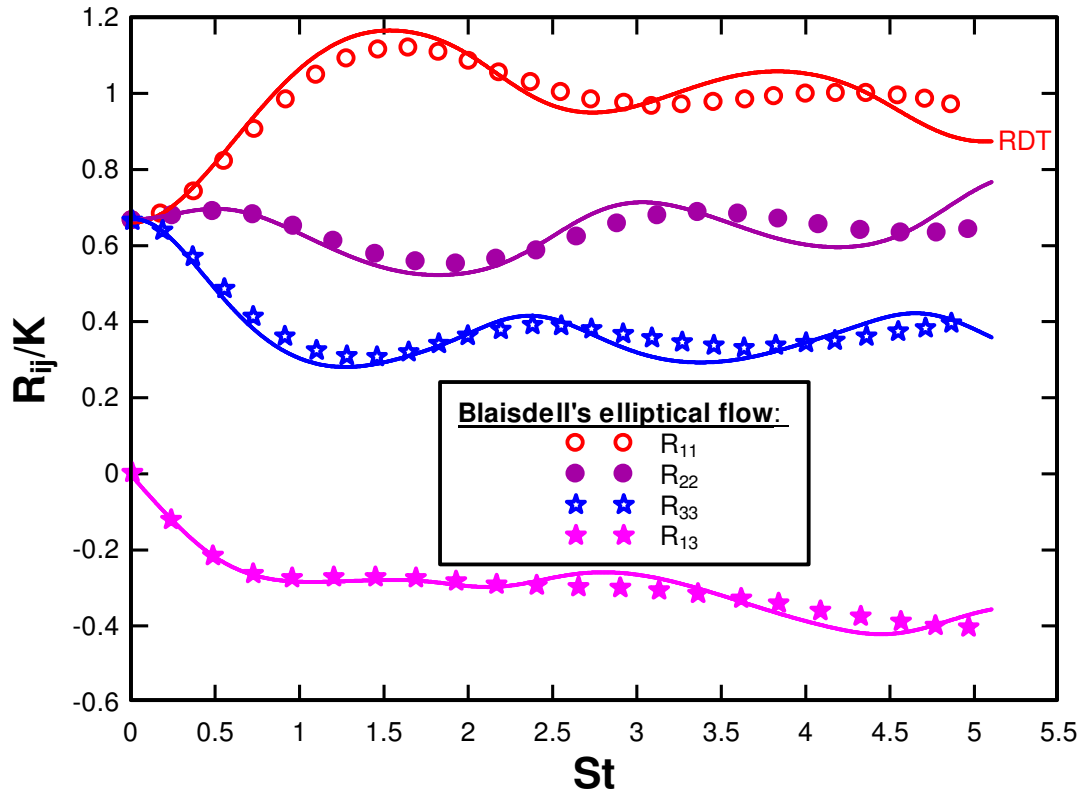


Figure 25: Blaisdell's elliptical flow: RDT

### 3.3. Return-to-Isotropy Model

For anisotropic cases, a term to model the return to isotropy behavior of turbulent flows was introduced. From equations (2.3.1), that term corresponds to the return-to-isotropy model for the Reynolds stresses. That is:

$$\left(\frac{1}{\tau_R}\right)D_{ij} \tag{3.3.1}$$

The oriented-eddy collision model includes two types of return representations:  $\hat{R}_{ij}$  and  $k$ -return.

### 3.3.1. $\hat{R}_{ij}$ -Return Model

Initially,  $D_{ij}$  was modeled in the following ways:

$$D_{ij}^A = \left( \frac{C_R}{1 + \frac{C_R}{\text{Re}}} \right) \left[ \hat{R}_{ij} - \hat{K} \left( \delta_{ij} - \frac{k_i k_j}{k^2} \right) \right] \quad (3.3.1.1)$$

$$D_{ij}^B = \left( \frac{C_R}{1 + \frac{C_R}{\text{Re}}} \right) \left[ \hat{R}_{ij} - \frac{K}{N} \left( \delta_{ij} - \frac{k_i k_j}{k^2} \right) \right] \quad (3.3.1.2)$$

$$D_{ij}^C = \left( \left( \delta_{il} - \frac{k_l k_i}{k^2} \right) \frac{R_{ls}}{K} \hat{R}_{sj} \left[ \frac{K^2}{R_{ls} R_{sl}} \right] + \left( \delta_{jl} - \frac{k_j k_l}{k^2} \right) \frac{R_{ls}}{K} \hat{R}_{si} \left[ \frac{K^2}{R_{ls} R_{sl}} \right] - \hat{R}_{ij} \right) \quad (3.3.1.3)$$

$$D_{ij}^D = \left[ \frac{K}{N} \frac{\hat{R}_{is} \hat{R}_{sj}}{\hat{R}_{nm} \hat{R}_{nm}} - \hat{R}_{ij} \right] \quad (3.3.1.4)$$

$$D_{ij}^E = \left( \frac{K^2}{R_{ls} R_{sl}} \frac{(R_{is} \hat{R}_{sj} + R_{js} \hat{R}_{si})}{K} - \hat{R}_{ij} \right) \quad (3.3.1.5)$$

The first two equations are modeled after Rotta's Reynolds Stress Transport (RST) return models. That is, both equations (3.2.2.1) and (3.2.2.2) work by relaxing each individual Reynolds stress towards an isotropic state (e.g. from an ellipse to a sphere) with ( $D_{ij}^B$ ) or without ( $D_{ij}^A$ ) regard to the other eddies. The only difference between the two equations is that one uses the individual kinetic energy of each eddy ( $\hat{K}$ ), while the second equation uses the average global kinetic energy ( $\frac{K}{N}$ ); thus we refer to  $D_{ij}^A$  as Rotta-L (Local Rotta) and  $D_{ij}^B$  as Rotta-G (global Rotta).  $C_R$  is a tuned constant that we determined as 4 in the case of Rotta-L and 2.5 for Rotta-G. Note that equations 3.2.2.3, 3.2.2.4 and 3.2.2.5 do not have a tunable constant; those were

generated by Perot & Chartrand<sup>8</sup>. With time, we hope to further explore the behavior of the last three equations, giving the fact that there are no tuning constants.

### 3.3.2. *K*-Return Models

This *k*-return model is part of the orientation equation (2.3.2) and corresponds to:

$$\left(\frac{1}{\tau_k}\right)m_i \quad (3.3.2.1)$$

The term  $m_i$  here was modeled two ways:

$$m_i^A = -\left(\frac{C_{K1}}{1 + \frac{18}{\text{Re}}}\right)\left(3\frac{k^2}{k^2}K_{ki} - \delta_{ki}\right)k_k \quad (3.3.2.2)$$

$$\text{with } \overline{k^2} = \frac{1}{N} \sum k^2 \quad (3.3.2.3)$$

$$\text{and } K_{ki} = \left(\frac{1}{N} \sum k_k k_i\right) / \left(\frac{1}{N} \sum k^2\right) \quad (3.3.2.4)$$

$$m_i^B = -\left(\frac{C_{K2}}{1 + \frac{18}{\text{Re}}}\right)\left(3\frac{k^2}{k^2}N_{ki} - \delta_{ki}\right)k_k \quad (3.3.2.4)$$

$$\text{with } N_{ki} = \frac{1}{N} \sum (k_k k_i / k^2) \quad (3.3.2.5)$$

The first equation is referred to as the “ $K_{ij}$  return model” while the second one is the “ $N_{ij}$  return model”.  $N_{ij}$  depends only on anisotropy in the orientations while  $K_{ij}$  also responds to anisotropy in the lengths of the eddies.  $C_{K1}$  and  $C_{K2}$  are tuning constants that we determined to be respectively 4 and 1. So far and based on numerous simulations, we determined  $K_{ij}$  to be the best performing return case as shown below in Figure 26.

At first it seems as the  $K_{ij}$ -return model performs better than the  $N_{ij}$ . However, looking closely, it is really difficult to come up with a conclusion.  $K_{ij}$  seems to work best on the  $R_{ii}$  terms while  $N_{ij}$  best performs on the non-diagonal elements. It is our goal to further investigate this as part of the future work.

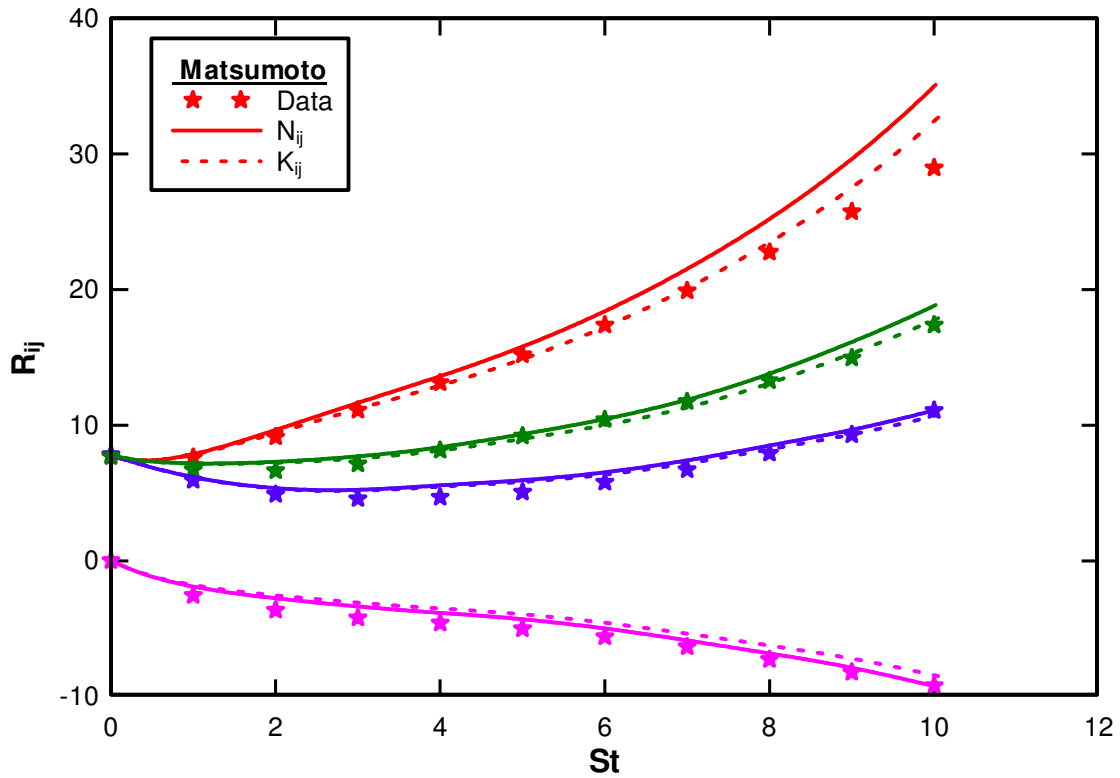


Figure 26:  $m_i^A$  and  $m_i^B$  model comparisons

As previously mentioned,  $(C_{K1}, C_{K2})$  are tuning constants that we determined to be respectively (4,10) for  $N_{ij}$ , and (1,4) for  $K_{ij}$ .

### 3.4. Shear/Strain Flows

In this section, we used various DNS as well as experimental cases to test our model performance; primary in the Reynolds stresses analysis of shear flows.

Tables 9 and 10 below provide a summary with the values of the constants  $C_R$  and  $C_K$ :

	Matsumoto <sup>16</sup>	Le Penven <sup>17</sup> A	Le Penven <sup>17</sup> B
<b>SK/ε</b>	4.71	0.43	0.33
<b>Re<sub>T</sub></b>	152	612	846
$(C_R, C_K)$	(4,10)	(4,10)	(4,10)
<b>Strain Tensor</b>	$\begin{pmatrix} 0 & 30 & 0 \\ 0 & 0 & 0 \\ 0 & 0 & 0 \end{pmatrix}$	$\begin{pmatrix} 5.48 & 0 & 0 \\ 0 & 1.99 & 0 \\ 0 & 0 & -7.47 \end{pmatrix}$	$\begin{pmatrix} 8.86 & 0 & 0 \\ 0 & -2.36 & 0 \\ 0 & 0 & 6.50 \end{pmatrix}$

Table 9: Matsumoto and Le Penven summary using (Rotta-L,  $K_{ij}$ ),  $(D_{ij}^A, m_i^A)$

	Hallback -PS		
<b>Re<sub>T</sub></b>	11		
$(C_R, C_K)$	(4,10)		
<b>SK/ε</b>	9	3	1
<b>Strain Tensor</b>	$\begin{pmatrix} 4.36 & 0 & 0 \\ 0 & -4.36 & 0 \\ 0 & 0 & 0 \end{pmatrix}$	$\begin{pmatrix} 1.46 & 0 & 0 \\ 0 & 0 & 0 \\ 0 & 0 & -1.46 \end{pmatrix}$	$\begin{pmatrix} 0.49 & 0 & 0 \\ 0 & 0 & 0 \\ 0 & 0 & -0.49 \end{pmatrix}$

Table 10: Hallback's summary using (Rotta-L,  $K_{ij}$ ) for Plane Strain  $(D_{ij}^A, m_i^A)$

### 3.5. Numerical Results: return-to-isotropy and shear/strain deformation

To illustrate the return-to-isotropy above, three different cases were used: Le Penven<sup>17</sup>, Matsumoto<sup>16</sup> and Hallback<sup>28</sup>. Only cases that are highly dependent on return-

to-isotropy were used to determine the values of our constants as well as to validate the models. All initial conditions are shown above in Tables 9 and 10. The results are shown in Figures 27 and 28.

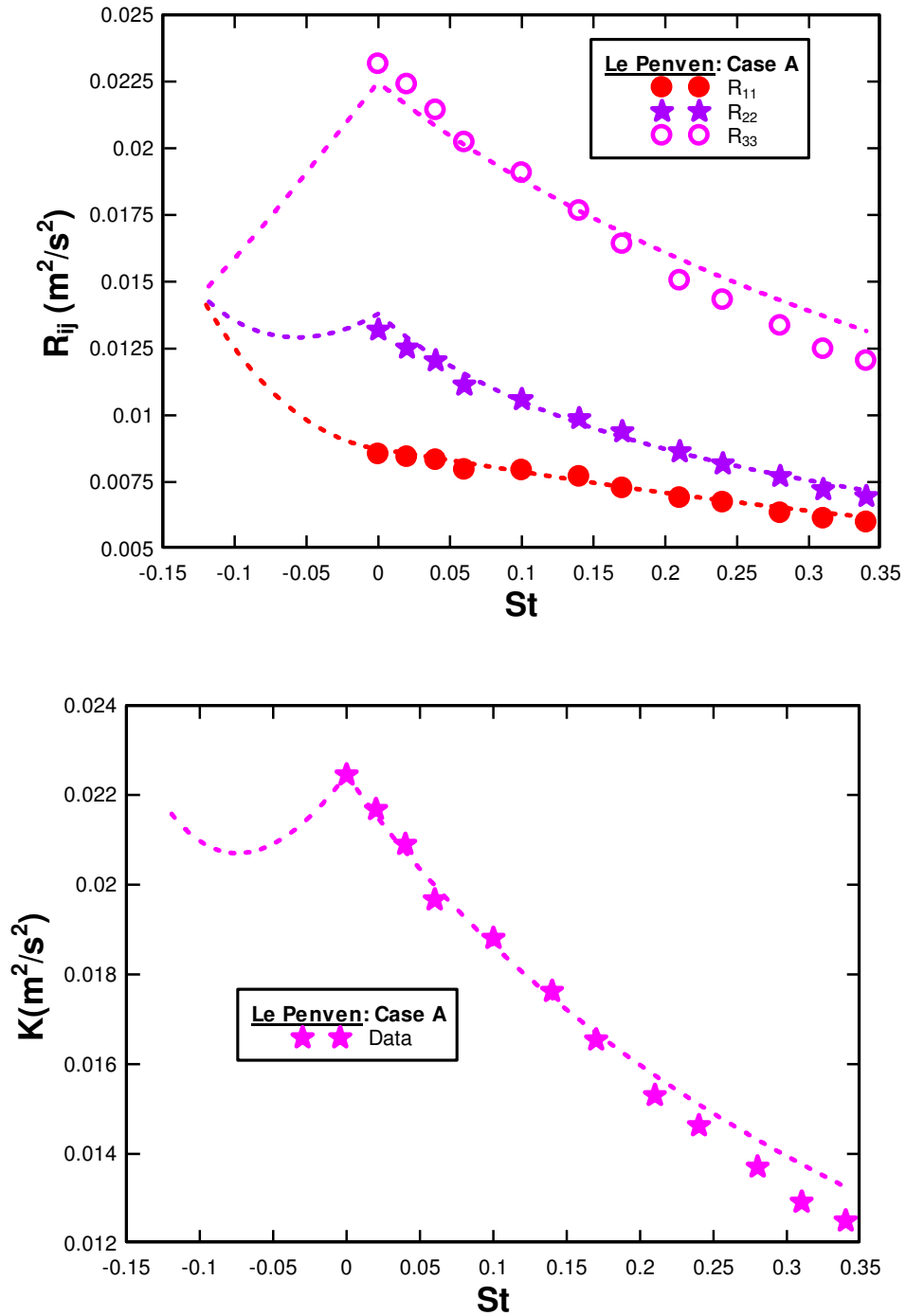


Figure 27: Le Penven - case A. a) Reynolds stresses and b) Kinetic energy

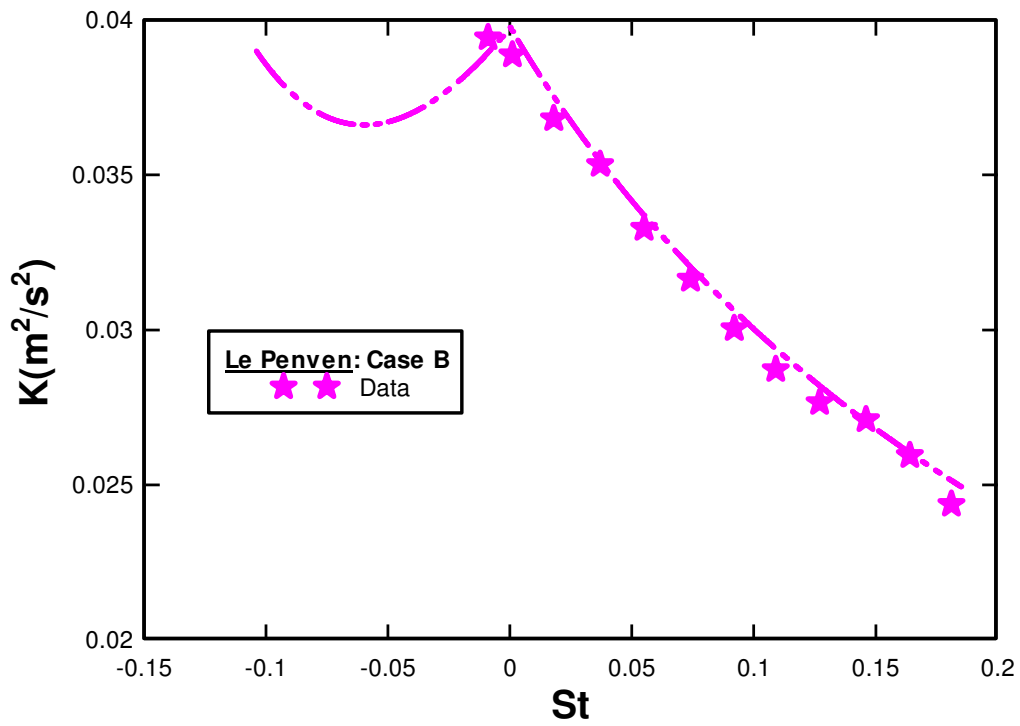
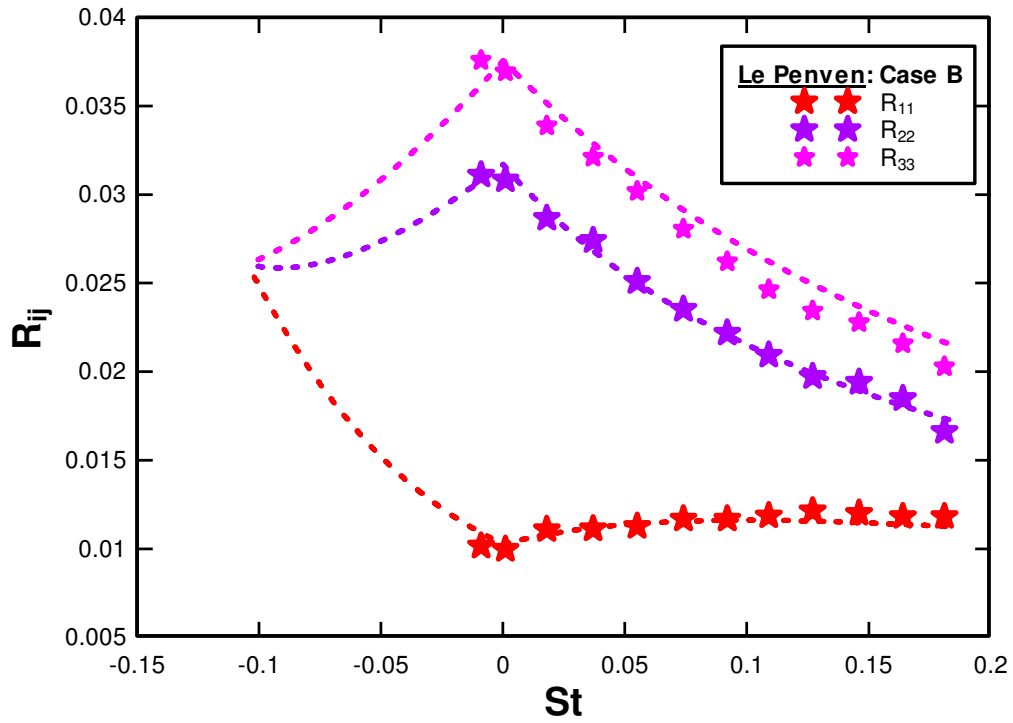


Figure 28: Le Penven - case B. a) Reynolds stresses and b) Kinetic energy

Correspondingly, the oriented-eddy collision prediction was compared to the homogeneous shear and strain flows: Matsumoto<sup>16</sup>, and Hallback<sup>28</sup> (PS):

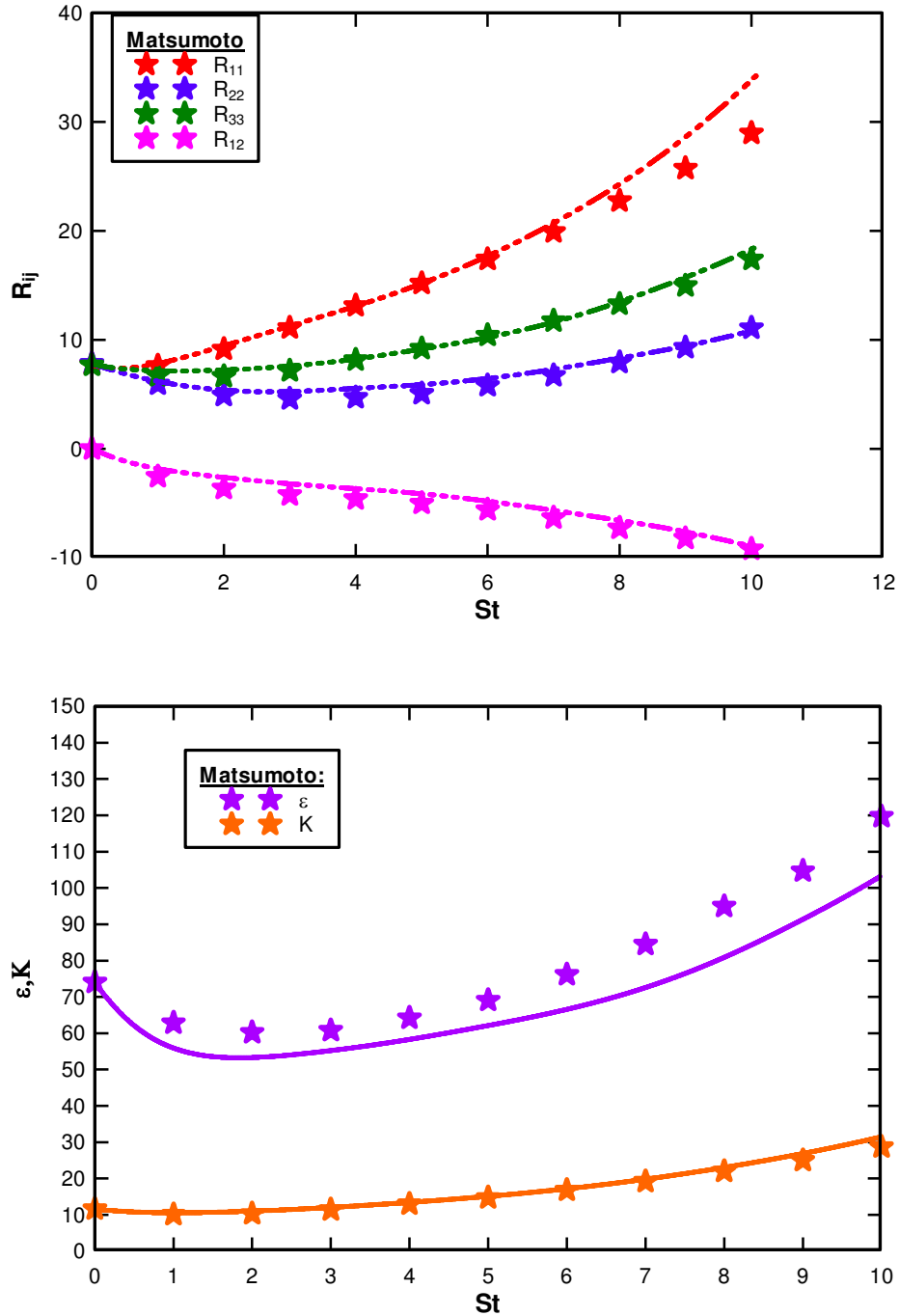


Figure 29: Matsumoto's shear deformation. The dots represent his DNS and the lines represent our model prediction. a) Reynolds stresses and b) Dissipation and kinetic energy

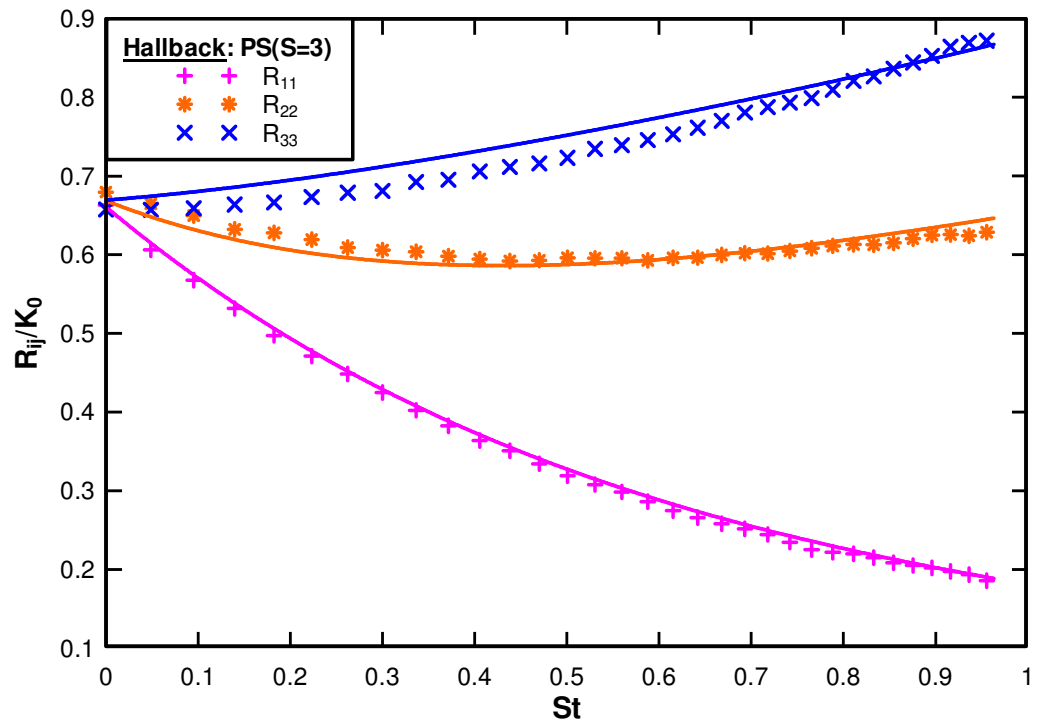
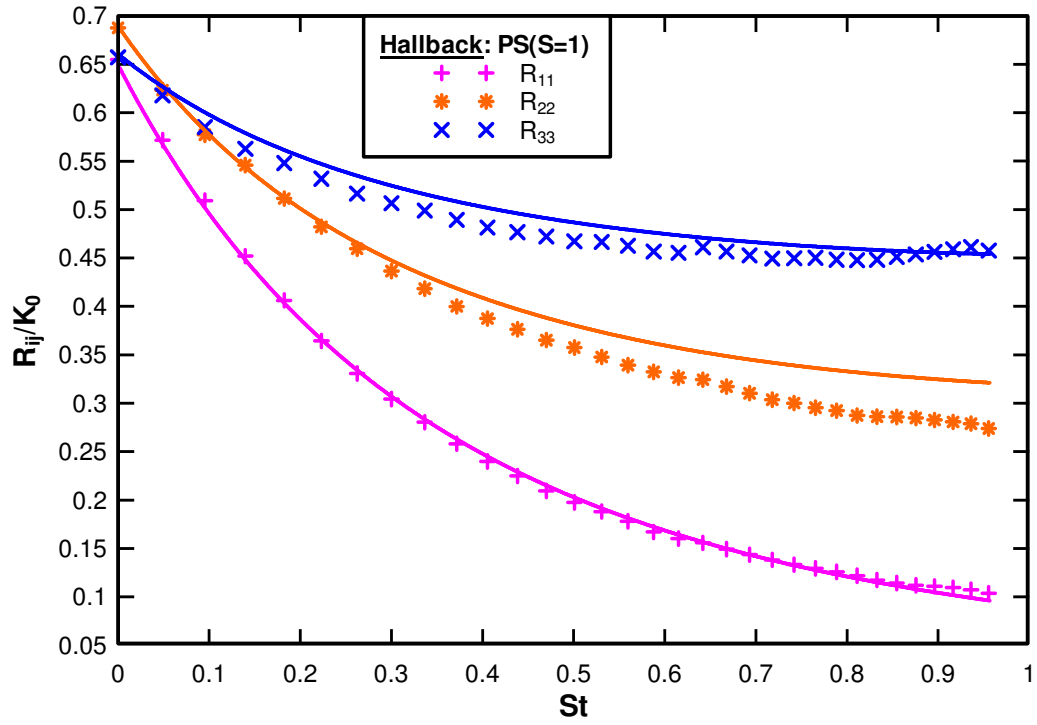


Figure 30: Hallback – Plane Strain a) S=1 and b) S=3

### 3.6. Diffusion

In equations (2.3.1) and (2.3.3), it was previously mentioned that the final term,  $\nabla\left((\nu + \nu_T)\nabla\hat{R}_{ij}\right)$  in equation (2.3.1) models the diffusive action of the Reynolds stresses while  $\nabla\left((\nu + \nu_T)\nabla k_i\right)$  accounts for the diffusive action of the orientation vectors  $k_i$ . In one-dimension,  $\nabla\left((\nu + \nu_T)\nabla\hat{R}_{ij}\right)$  corresponds to

$$\frac{\partial}{\partial y}\left(\nu + \nu_t\right)\frac{\partial\hat{R}_{ij}}{\partial y} \quad (3.6.1)$$

$\nu$  is the fluid viscosity while  $\nu_t$  corresponds to the eddy viscosity. We defined local and global eddy viscosities. As mentioned before, “local” implies that all calculations are done locally. In this case, the model uses a local  $\nu_t$  that is defined as

$$\nu_t^L = C_L \frac{(\hat{K})^2}{\varepsilon} \quad (3.6.2)$$

$$\text{with } \hat{K} = \frac{1}{2}\hat{R}_{ii} \quad (3.6.3)$$

$$\text{and } C_L = 1 \quad (3.6.4)$$

Regarding the global eddy viscosities, two equations that are referred to as *global1* and *global2* ( $\nu_t^{G1}$  and  $\nu_t^{G2}$ ) are currently being evaluated. The *global1* and *global2* are similar, with the only difference that in the first case, the local kinetic energy and dissipation are being summed *before* dividing, whereas in the second case, the summation is done *after* the division. These concepts are illustrated below in equations (3.6.5) and (3.6.6):

$$\nu_t^{G1} = C_{G1} \frac{1}{N} \left[ \frac{\Sigma(\hat{K}^2)}{\Sigma(\varepsilon)} \right] \quad (3.6.5)$$

$$\nu_t^{G2} = C_{G2} \frac{1}{N} \left[ \Sigma \left( \frac{\hat{K}^2}{\varepsilon} \right) \right] \quad (3.6.6)$$

where  $C_{G1} = C_{G2} = 1$  and  $\Sigma$  implies “summation over the orientations”.

As expected for isotropic flows (the orientations vectors all have then same length), both global eddy viscosity formulas ( $\nu_t^{G1}$  and  $\nu_t^{G2}$ ) performed equally as shown in Figure 31 below. The comparison was done using the DNS of Carati<sup>58</sup>:

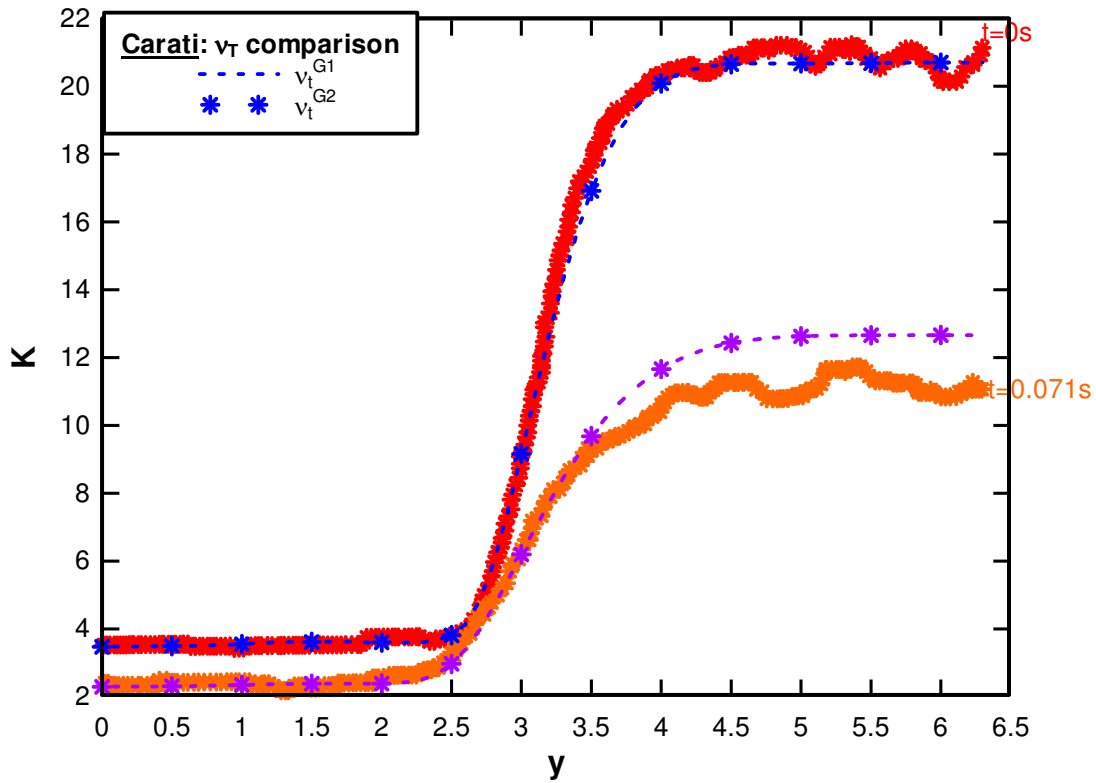


Figure 31: Eddy viscosity comparison for both global equations

After implementing the diffusion (equation 3.6.1) in the source code along with all three variants of the eddy viscosity (equations 3.6.2, 3.6.5 and 3.6.6), various simulations were conducted in order to determine the efficacy of the eddy collision model. It is important to mention that the kinetic energy decay is no longer homogeneous (as previously) but instead is also spatially dependent. In the diffusion case, at one fixed time  $t$ , we are looking at both the kinetic energy and dissipation at different locations ( $y$ ). The first step in the analysis is to determine which eddy viscosity equation best models the diffusion process. Starting with  $v_t^{G1}$  (eq 3.6.5), various simulations were conducted as part of the evaluation process. The first simulation was run against that of Chasnov<sup>23</sup> and shows the diffusion process at different times  $t$ . Chasnov's flow is inhomogeneous with the following characteristics: shearless, irrotational and isotropic with periodic boundary conditions. Note that in order to reduce the time step, we interpolated the original data as represented by the solid blue line.

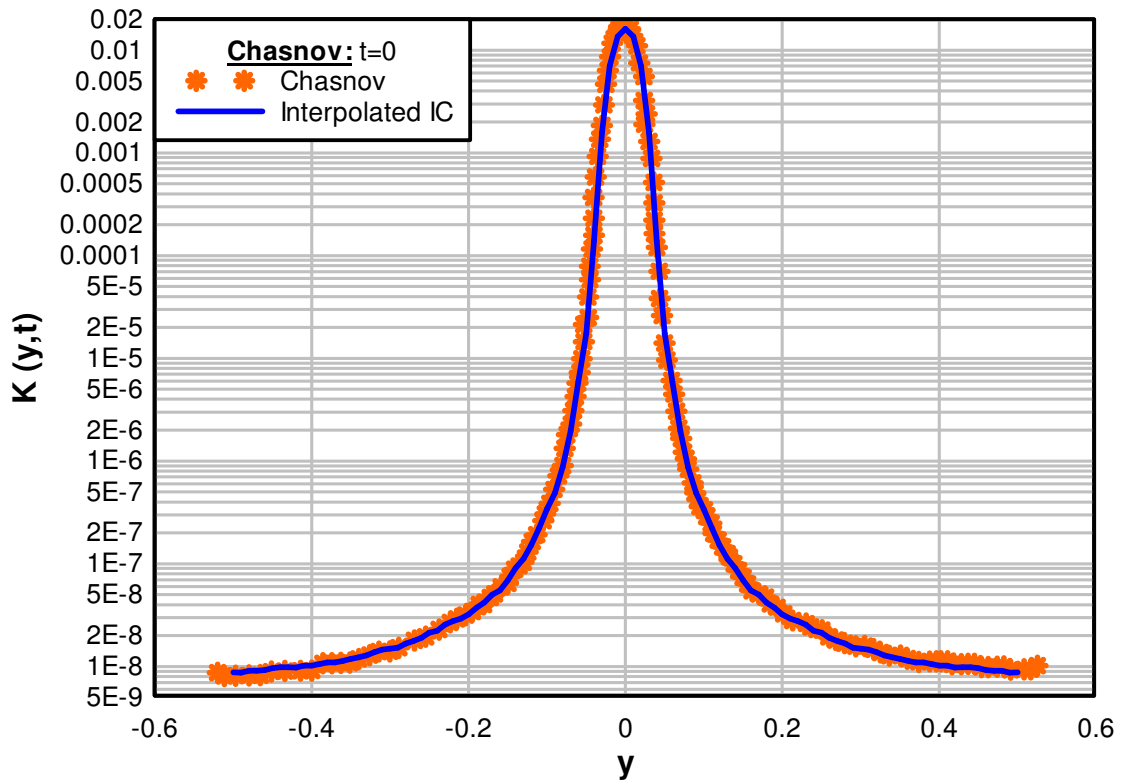


Figure 32: Kinetic energy versus position at different times  $t$ . Chasnov at  $t=0$ . The stars represent data from Chasnov and the solid blue line corresponds to our interpolation.

Next in Figure 33, we looked at the diffusion evolution at times  $t=1.375, 4.125$  and  $9.625$  seconds. The asterisks represent the data and the matching solid blue lines correspond to our simulations.

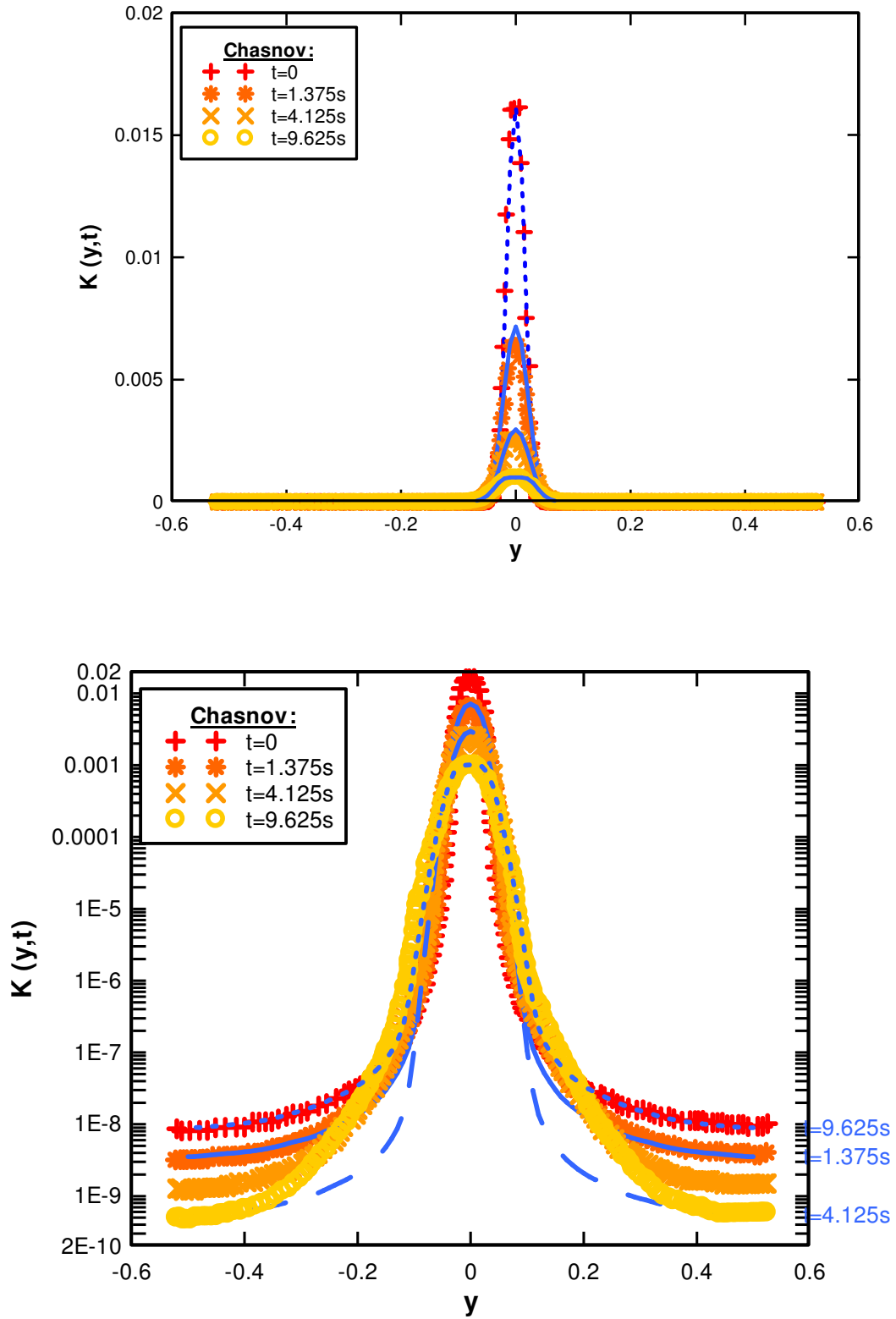


Figure 33: Kinetic Energy versus position at different times  $t$ . The matching blue lines correspond to the OEC simulations. a) linear-linear plot and b) log-linear plot.

The second diffusion simulation matched that of Barry Gilbert<sup>59</sup>. Gilbert assumes a shearless, irrotational and homogeneous flow. In addition, the flow has some levels of anisotropy. The stars represent data from Gilbert at times  $t=0, 0.0292, 0.0402, 0.0764, 0.0884, 0.1154, 0.1274, 0.1634$  and  $0.2024$  seconds. The matching solid lines correspond to the simulations.

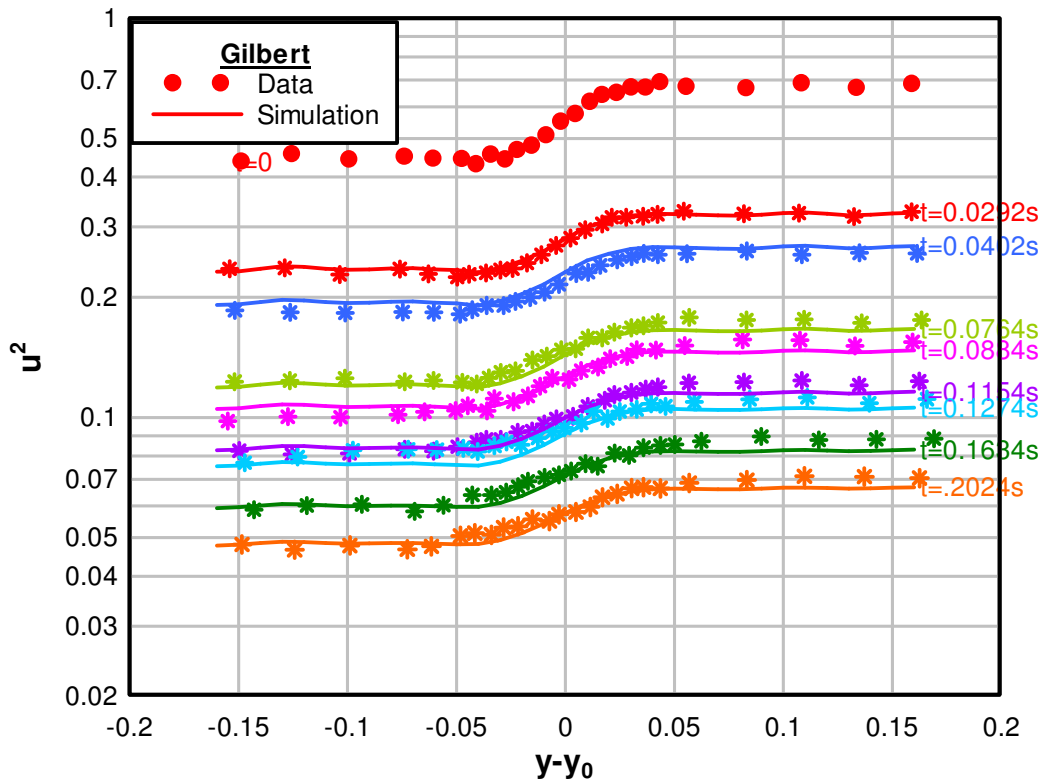


Figure 34:  $R_{11}$  (kinetic energy component) versus position. The stars represent data from Gilbert at times  $t=0, 0.0292, 0.0402, 0.0764, 0.0884, 0.1154, 0.1274, 0.1634$  and  $0.2024$  seconds. The matching solid lines correspond to the OEC simulations.

The final set of data that was looked at is more recent one (2002) and was published by Carati<sup>58</sup>. Carati's data is unique in a sense that we have access to both the kinetic energy and the dissipation rate. Here although not ideal, we used zero boundary conditions

compared to periodic conditions in the two cases above (Chasnov, Gilbert). For reasons that remain unclear at this time, the OEC isotropic simulations decay a little faster than expected. The results obtained are shown below in Figures 35 and 36:

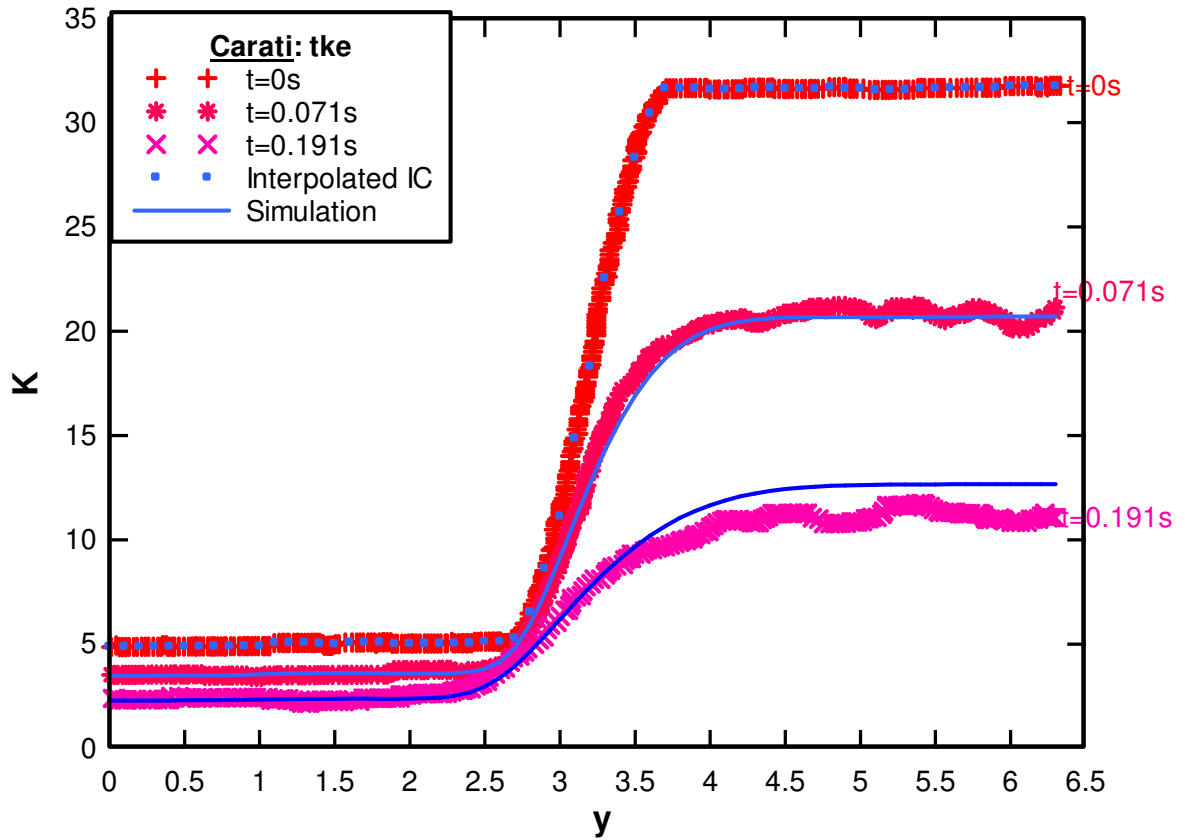


Figure 35: Kinetic Energy versus position at different times  $t$ . The stars represent data from Carati at times  $t=0, 0.071$  and  $0.191$  seconds. The matching solid lines correspond to our simulations.

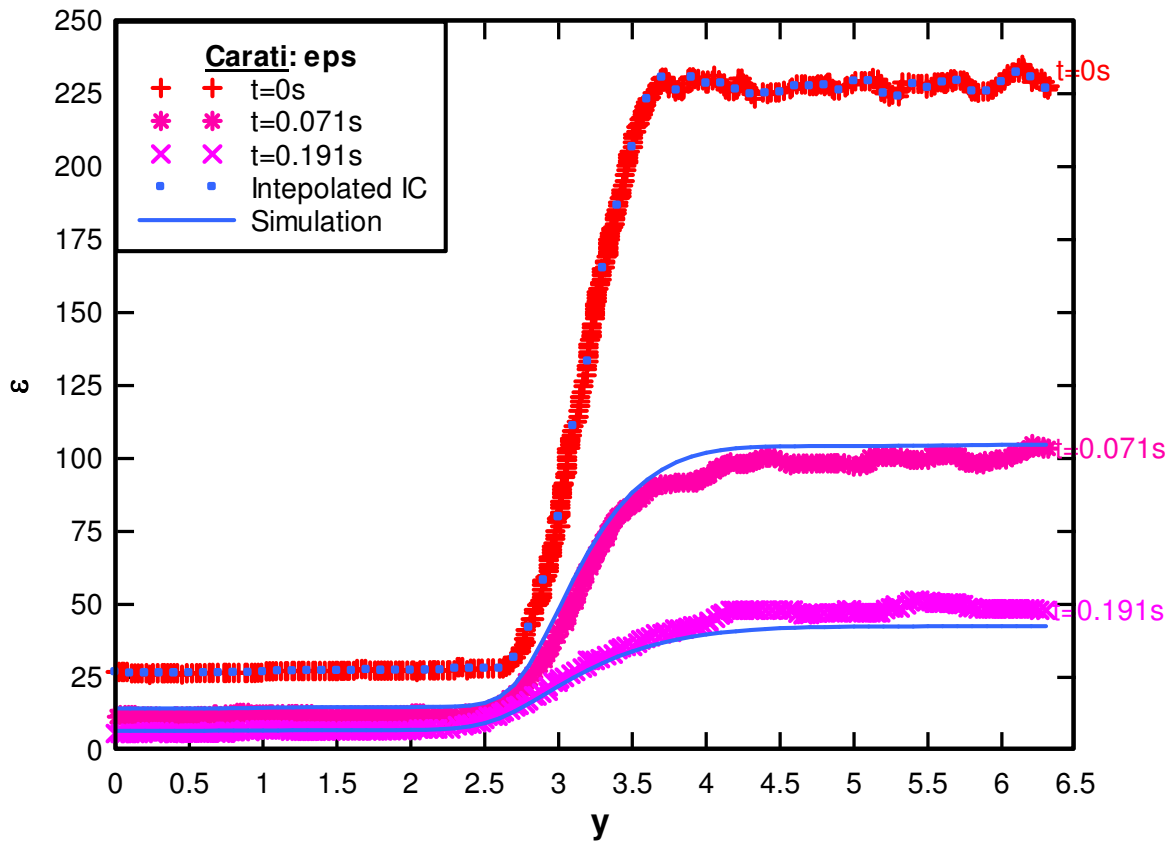


Figure 36: Dissipation versus position at different times  $t$ . The stars represent data from Carati at times  $t=0, 0.071$  and  $0.191$  seconds. The matching solid lines correspond to our simulations.

## CHAPTER 4

### CONCLUSIONS

This project has allowed us to demonstrate that oriented-eddy collisional (OEC) models are an interesting, accurate, and viable approach to turbulence modeling. We have demonstrated that:

- Models exist in the regime between LES and RANS that have very attractive cost and accuracy attributes for current day design.
- It is possible to increase the physics in turbulence models and reduce the number of tuned constants, while still having a cost effective model that can run on a PC.
- The structure (orientation) of turbulence is just as important as the magnitude of the fluctuations. Models that represent structure have huge advantages in capturing the turbulence physics.
- The model can be interpreted as a model for the evolution of the two-point correlation. Critical to this model – is decomposing the two-point correlation into self-similar ‘modes’.

As with any turbulence model, a great deal of work remains to validate this model. In this project we have clearly demonstrated that the approach is extensible and can accurately predict a wide variety of quite different but fundamental turbulent flow situations.

Future work will complete the modeling of wall effects. In addition, we expect this model to predict transition very well, and this will be demonstrated. Finally, this model will be implemented in a 3D, unstructured, parallel, Navier-Stokes code so that more complex and practical flow situations can be tested.

## REFERENCES

1. J. Rotta, "Statische theorie nichthomogener turbulenz I," *Z. für Physik* **129**, 547-572 (1951).
2. J. L. Lumley, "Computation modeling of turbulent flows", *Advances in Applied Mechanics* **18**, 126-176. (1978).
3. S. Sarkar and C. G. Speziale, "A Simple Nonlinear Model for the Return to Isotropy in Turbulence," *Physics of Fluids*, Vol. A2, No. 1, pp. 84-93 (1990).
4. K. S. Choi and J. L. Lumley, "Turbulence and Chaotic Phenomena in Fluids," *Proceedings of the IUTAM Symposium* (Kyoto, Japan), edited by T. Tatsumi, North-Holland, Amsterdam, p. 267, (1984).
5. K. S. Choi and J. L. Lumley, "The return to isotropy of homogeneous turbulence," *J. Fluid Mech.*, Vol. 436, pp 57-84 (2001).
6. C. G. Speziale, S. Sarkar and T. B. Gatski, "Modeling the pressure-strain correlation of turbulence: an invariant dynamical systems approach," *J. Fluid Mech.*, Vol. 227, pp 245-272 (1991)
7. G. A. Blaisdell & K. Shariff, "Simulation and modeling of the elliptic streamline flow". *Proceedings of the 1996 Summer Program*, Center for Turbulence Research, NASA Ames/Stanford Univ., 443-446, (1996)
8. J. B. Perot & C. Chartrand, "Modeling Return to Isotropy Using Kinetic Equations," accepted to *Phys. Of Fluids*, (2004)
9. J. B. Perot and P. Moin, "A Near Wall Model for the Dissipation Tensor," Eleventh Australasian Fluid Mechanics Conference, Hobart, Tasmania, Australia, 13-18 (1992).
10. S. B. Pope, *Turbulent Flows*, Cambridge University Press, 2000.
11. S. Tavoularis and S. Corrsin, "Experiments in nearly homogeneous turbulent shear flow with a uniform mean temperature gradient. Part1," *J. Fluid Mech.* **104**, 311-347 (1981).
12. P. K. Yeung and S. B. Pope, "Lagrangian statistics from direct numerical simulations of isotropic turbulence," *J. Fluid Mech.*, **207**, 531-586 (1989)
13. P. G. Saffman, "Note on decay of homogeneous turbulence," *Physics of fluids* **10**, 1349, (1967).
14. M. Oberlack, "Non-isotropic dissipation in non-homogeneous turbulence", *J. Fluid Mech* 350, 351-374 (1997)

15. M. J. Lee and W. C. Reynolds, "Numerical experiments on the structure of homogeneous turbulence," Stanford University Tech. Rep TF-24 (1985).
16. Matsumoto, A., Nagano, Y. and Tsuji, T., "Direct Numerical Simulation of Homogeneous Turbulent Shear Flow," 5th Symposium on Computational Fluid Dynamics, 1991, pp. 361-364.
17. L. Le Penven, J. N. Gence, and G. Comte-Bellot, "On the Approach to Isotropy of Homogeneous Turbulence: Effect of the Partition of Kinetic Energy Among the Velocity Components", *Frontiers in Fluid Mechanics*, 1-21 (1985).
18. W. C. Reynolds & S. C. Kassinos, A one-point model for the evolution of the Reynolds stress and structure tensors in rapidly deformed homogeneous turbulence, *Proc. R. Soc. London, Ser A* **451**, 87, 1995.
19. P. R. Van Slooten & S. B. Pope, PDF modeling for inhomogeneous turbulent with exact representation of rapid distortions, *Phys. Fluids*, **9**, 1085, 1997.
20. S. M. de Bruyn Kops & J. J. Riley, Direct numerical simulation of laboratory experiments in isotropic turbulence, *Phys. Fluids*, **10** (9), 2125-2127, 1998.
21. G. Comte-Bellot & S. Corrsin, Simple Eulerian time correlation of full and narrow-band velocity signals in grid-generated, 'isotropic' turbulence, *J. Fluid Mech.* **48**, 273, 1971.
22. J. B. Perot & S. Natu, A model for the dissipation tensor in inhomogeneous and anisotropic turbulence, Submitted to *Phys. Fluids*, May 2003.
23. J. R. Chasnov, "Decaying Turbulence in Two and Three Dimensions" in *Advances in DNS/LES*, edited by C. Liu and Z. Liu, (1997)
24. N. N. Mansour and A. A. Wray, "Decay of Isotropic turbulence at low Reynolds number," *Physics of Fluids*, Volume 6, Issue 2, , pp.808-814, February (1994)
25. N. Kolmogoroff, "The local structure of turbulence in incompressible viscous fluid for very large Reynolds number," *Dokl. Akad. Nauk SSSR*, **30**, 301-305 (1941).
26. S. G. Saddoughi and S. V. Veeravalli, "Local isotropy in turbulent boundary layers at high Reynolds number," *J. Fluid Mech.* **268**, 333 -372 (1994).
27. W. K. George & H. J. Hussein, "Locally axisymmetric turbulence", *J. Fluid Mech.* **233**, 1-23 (1991).
28. M. Hallbäck, J. Groth & A. V. Johansson, "A Reynolds stress closures for the dissipation in anisotropic turbulent flows," 7<sup>th</sup> Symposium on Turbulent Shear Flows, Stanford University, August. (1989).

29. M. Hallböck, J. Groth & A. V. Johansson, "An algebraic model for nonisotropic turbulent dissipation rate in Reynolds stress closures," *Phys. Fluids*, **2** (10), 1859-1866, (1990).
30. P. A. Durbin and C. G. Speziale, "Local anisotropy in strained turbulence at high Reynolds numbers", *ASME J. Fluids Eng.* **113**, 707-709 (1991).
31. J. L. Lumley and G. R. Newman, "The return to isotropy of homogeneous turbulence," *J. Fluid Mech.* **82**, 161-178 (1977).
32. N. N. Mansour, J. Kim & P. Moin, "Reynolds-stress and dissipation-rate budgets in a turbulent channel flow," *J. Fluid Mech.* **194**, 15-44 (1988).
33. M. Hallböck, A. V. Johansson and A. D. Burden, "Transition and turbulence modeling," Hallböck, Johansson, Henningson & Alfredsson, eds., Kluwer Academic Publishers, 81-154, (1996).
34. B. E. Launder and B. L. Li, "On the elimination of wall topography parameters from second moment closure," *Phys. Fluids* **6**, 537-566 (1994).
35. C. G. Speziale and T. B. Gatski, "Analysis and modeling of anisotropies in the dissipation rate of turbulence," *J. Fluid Mech.* **344**, 155-180 (1997).
36. J. B. Perot "Shear-Free Turbulent Boundary Layers: Physics and Modeling," Ph.D Thesis, Stanford University Tech. Report TF60 (1993).
37. W. C. Reynolds, "Physical and analytical foundations, concepts, and new directions in turbulence modeling and simulation," In *Turbulence Models and their Applications*. Editions Eyrolles, 61 Bd Saint-Germain Paris 2 (1984).
38. S. G. Speziale, "Analytical methods for the development of Reynolds stress closure in turbulence," *Annual Review of Fluid Mechanics* **23**, 107-157 (1991)
39. J. B. Perot and P. Moin, "Shear-Free Turbulent Boundary Layers, Part I: Physical Insights into Near Wall Turbulence," *J. Fluid Mech.* **295**, 199-227 (1995).
40. J. B. Perot & P. Moin, "Shear-Free Turbulent Boundary Layers, Part 2: New concepts for Reynolds stress transport equation modelling of inhomogeneous flows," *J. Fluid Mech.* **295**, 229-245 (1995).
41. R. D. Moser, J. Kim and N. Mansour, "Direct numerical simulation of turbulent channel flow up to Re=590" *Phys. Fluids.* **11**, 943-945, (1999)
42. Kristoffersen, R., Andersson, H.I. 1993 "Direct simulations of low-Reynolds-number turbulent flow in a rotating channel" *J. Fluid Mech.*, **256**, 163-197.
43. H. Le, P. Moin, and J. Kim, "Direct numerical simulation of turbulent flow over a backward-facing step," *J. Fluid Mech.* **330**, 349-374, (1997).

44. S. Natu, "A Reynolds stress transport model for the near wall region," Masters Thesis, University of Massachusetts, Amherst, (2003).
45. S. B. Pope, Lagrangian PDF methods for turbulent flows. *Annual Rev. Fluid Mech.* **26**, 23-63, 1994.
46. W. C. Reynolds, Effects of rotation on homogeneous turbulence, Proceedings of the 10<sup>th</sup> Australasian Fluid Mechanics Conference, University of Melbourne, Australia, 1989.
47. J. B. Perot & R. Nallapati, A Moving Unstructured Staggered Mesh Method for the Simulation of Incompressible Free-Surface Flows, *Journal of Computational Physics*, **184**, 192-214, 2003.
48. P.A. Durbin, Near-wall turbulence closure modeling without ‘damping functions’, *Theoret. Comput. Fluid Dynamics* **3**, 1-13, 1991. Using the Turbulent Potential Model, *Journal of Turbulence*, **3**, January. 2002.
49. S.A Orzag, V. Yakhot, W.S. Flannery, F. Boysan, D. Choudhury, J. Marusewski and B. Patel, B., Renormalization group modeling and turbulence simulations", So, R.M.C., Speziale, C.G. and Launder, B.E. (eds.), Near-wall turbulent flows. Elsevier Science Publisher, 1993
50. O. Reynolds, On the dynamical theory of viscous incompressible fluids and the determination of the criteria, *Philos. Trans. R. Soc. London A* **186**, 123-161, 1895.
51. W. Chang & J. B. Perot, Prediction of Turbulent Transition in Boundary Layers R. S. Rogallo and P. Moin, Numerical simulation of turbulent flows, *Annual Rev. Fluid Mech.* **16**, 99-137, 1984.
52. M. Germano, Turbulence: the filtering approach, *J. Fluid Mech.*, **238**, 325-336, 1992.
53. P. R. Spalart, Strategies for turbulence modeling and simulations, *Engineering Turbulence Modelling and Experiments* 4, Rodi and Laurence, eds. Elsevier, 1999.
54. Von Karman, T. & Howarth, L. 1938, "On the statistical theory of isotropic turbulence", *Proc. Royal Soc. London Ser. A*, **164**, 192.
55. Yu, H., Girimaji, S. S. & Luo, L.-S., 2005, "DNS and LES of decaying isotropic turbulence with and without frame rotation using a lattice Boltzmann method", *J. Comput. Phys.*, **209**, 599-616.
56. M. Yamamoto and C. Arakawa, "Study on the Pressure-Strain Term in Reynolds Stress models." *Proceedings of the Eighth Symposium on Turbulent Shear Flows*, Technical University of Munich, Munich, Germany, pp. III-17-1 – III-17-2 (1991).

57. D. Carati, G. Winckelmans, H. Jeanmart, On the modelling of the subgrid-scale and filtered-scale stress tensors in large-eddy simulation, *J. Fluid Mech.* **441** (2001) 119-138.
58. G. Winckelmans, H. Jeanmart, D. Carati, On the comparison of turbulence intensities from large-eddy simulation with those from experiment or direct numerical simulation, *Phys. Fluids* **14** (2002) 1809-1811.
59. B.Gilbert, Diffusion mixing in grid turbulence without mean shear, *J. Fluid Mech.* **100** (1980) 349-365.
60. Squires (LES)- See Table 2, on Page 31
61. Jacquin (Exp. Data)- See Table 2, on Page 31, and then P. 34,38,39,43,45
62. Mansour, cambon & Spezia -See Table 2, on P. 31, and then P. 33, 38, 41, 42, 43,48.
63. Wigeland & Nagib, See Table 2, on Page 31, 32, 39, 43, 44.
64. C. Chartrand, “Eddy Collision Model for Turbulence”, Masters Thesis, University of Massachusetts, Amherst, (2005)
65. de Bruyn Kops, Private Correspondance
66. Shimomura- See Table 6 , on Page 39, 43, 45, 46
67. Veeravalli, unpublished